

Design of Circuits & Systems for Healthcare Sensing Application

Thesis submitted in partial fulfilment
of the requirements for the degree of

*(Master of Science in **Electronics and Communication Engineering** by Research)*

by

Arpit Sahni

2021702009

arpit.sahni@research.iiit.ac.in



International Institute of Information Technology

Hyderabad - 500 032, INDIA

March 2024

Copyright © Arpit Sahni,
March 2024.
All Rights Reserved

International Institute of Information Technology
Hyderabad, India

CERTIFICATE

It is certified that the work contained in this thesis, titled “*Design of Circuits & Systems for healthcare sensing application*” by Arpit Sahni, has been carried out under my supervision and is not submitted elsewhere for a degree.

Date

Advisor: Dr. Abhishek Srivastava.

To the Past, Present and Future

Acknowledgments

I want to convey my deep and heartfelt gratitude to all those who have been an integral part of my journey in completing my master's thesis. First and foremost, I am immensely thankful to my dedicated thesis advisor, **Dr. Abhishek Srivastava**. His mentorship, patience, and unwavering support have played a pivotal role in shaping this work. Dr. Srivastava's insightful feedback and expert guidance have not only been instrumental but also truly inspiring throughout this academic endeavor.

To my family, I extend my sincere appreciation for their unwavering encouragement and steadfast belief in my abilities. Their love and unwavering support have served as the foundation of strength that has carried me through this challenging journey.

I would also like to express my gratitude to my lab-mates specifically **Srayan Sankar Chatterjee, Anushka Tripathi, Deeksha, Pranjal Mahajan** and **Srikar Somanchi**. Their presence has created a supportive network that has offered valuable insights and a sense of camaraderie during this demanding yet ultimately rewarding period of my academic life.

To my dearest friends **Neha S, Chetan Mittal and Ashish Papreja**, whose unwavering support and encouragement have been instrumental in my journey, I extend my heartfelt gratitude. Your belief in my abilities and your unwavering presence throughout this endeavour has been a source of strength and inspiration. Thank you for being my pillars of support and for sharing in the joys and challenges of this journey.

Lastly, I am profoundly thankful to the academic and administrative staff at IIIT Hyderabad for their indispensable assistance and the resources they provided, which were crucial to the successful completion of this thesis.

This thesis project would not have been possible without the collective contributions of these exceptional individuals and institutions. I genuinely appreciate each and every one of you for being an integral part of this significant chapter in my academic journey. Your support and guidance have been invaluable, and I am deeply grateful for your unwavering belief in my capabilities.

Abstract

The recent surge in healthcare sensing technologies has revolutionized the landscape of patient care and safety monitoring. This thesis delves into the burgeoning field of healthcare sensing and addresses the critical need for advancements in monitoring systems applicable to various domains, including elderly care, critical care units, and prolonged home monitoring. These applications necessitate the continuous and non-intrusive measurement of vital signs such as heart rate, blood-oxygen saturation, temperature, and subject movement.

This research focuses on enhancing patient comfort and convenience by introducing innovative solutions. Firstly, the thesis introduces a receiver front-end integrated circuit (IC) tailored for radar systems enabling non-contact-based measurement of vital signs. This radar-based approach offers a non-invasive method for obtaining crucial health parameters, promising increased accuracy and reliability while minimizing patient discomfort.

Furthermore, in response to the growing demand for portable safety systems in industrial settings, the thesis presents the development of a portable industry safety system. This system is designed to provide comprehensive safety monitoring in industrial environments, ensuring the well-being of workers through real-time monitoring and hazard detection.

Through the exploration of these technological advancements, this thesis contributes to the field of healthcare sensing and safety systems. The proposed receiver front-end IC for radar-based vitals monitoring offers a novel approach to non-contact sensing, while the portable industry safety system aims to enhance workplace safety through continuous monitoring and hazard detection. Overall, these advancements pave the way for improved healthcare monitoring and industrial safety, addressing critical needs in both domains.

Contents

Chapter	Page
1 Introduction	1
1.1 Objectives and contributions	2
1.2 Thesis Organisation	3
2 Design of a Wideband 8-20 GHz Receiver Front-End with Reduced Local Oscillator Phase-Error in 4-Path Mixer	4
2.1 Introduction	4
2.2 N-path RxFE at High Frequencies : Equivalent Model and Design Challenges	5
2.2.1 Equivalent LTI model of N-Path RxFE	5
2.2.2 Design Challenges of 4-path RxFE at high frequency (>10 GHz)	7
2.2.2.0.1 LO phase matching	7
2.2.2.0.2 RF input matching	7
2.3 Design consideration and implementation of wideband 4-path RxFE	8
2.3.1 LO Generation	8
2.3.2 Matching network design for 4-path mixer	9
2.3.3 IF Amplifier	10
2.4 Simulation Results	11
2.5 Conclusion	13
2.6 Measurement circuit for the proposed topology in TSMC 65 nm technology node	13
3 Design of Integrated System for Detection of Micro-organisms with Fabrication and Testing of ZnO Nanorods based Biosensor	17
3.1 Introduction	17
3.2 Proposed sensor and interface-circuit for micro-organism detection	18
3.3 Considerations for EIS Circuit Design	20
3.3.1 EIS circuit design consideration	21
3.4 Implementation details and Measurement results	22
3.4.1 Sensor Fabrication and SEM results	22
3.4.2 EIS implementation and Characterization	24
3.4.3 System prototype	24
3.5 Conclusion	25
4 <i>GoldAid</i> : Industry Safety System for Enabling Rapid Medical <i>Aid</i> in the <i>Golden Hour</i>	26
4.1 Introduction	26
4.2 System Overview and Architecture Details	28

4.2.1	Wearable Safety Device (WSD)	28
4.2.1.1	Sense module	28
4.2.1.2	Core module	29
4.2.1.3	Communication module	29
4.2.2	Base Station Device (BSD)	29
4.2.3	IoT connectivity and application interface for CMS	29
4.3	Proposed Fall detection Methods	30
4.3.1	Test Hardware and Experiments for Data Collection	30
4.3.2	Algorithm-1: Machine Learning (ML) approach	32
4.3.3	Algorithm-2: Acceleration-threshold approach	33
4.4	Hardware Implementation	36
4.4.1	Sense Module	36
4.4.1.1	Fall detection	36
4.4.1.2	Live tracking and Hazardous zone detection	37
4.4.1.3	Vitals	37
4.4.2	Core Module	38
4.4.3	Communication Module	38
4.5	Measurement Results	39
4.5.1	Individual Module testing	39
4.5.1.1	Measurement results for fall detection	39
4.5.1.2	Communication range testing and power consumption	40
4.5.2	Full system testing in a live environment	42
4.6	Conclusion	43
5	Conclusions and Future Work	44
5.1	Research Contributions	44
5.2	Future Works	45

List of Figures

Figure	Page
1.1 High-level architecture of the vital measurement using FMCW radar	1
2.1 Depiction of an N-path mixer based RxFE and its LO phases	5
2.2 Block diagram of 4-path Mixer	6
2.3 (a) LTI equivalent circuit of 4-path Mixer (b) Variation of input resistance with varying R_{BB}	7
2.4 Block diagram of full Receiver front-end	8
2.5 (a) Quadrature error vs LO frequency (b) Transient plot of Quadrature LO pulses	9
2.6 (a) LTI equivalent circuit of 4-path Mixer with matching network (b) Plot of S_{11} vs Frequency for different R_{bb} values	10
2.7 (a) Fully differential OTA used as IF amplifier in TIA configuration (b) Layout of the proposed receiver front-end in TSMC 65nm	11
2.8 Plot by varying frequency for (a) IIP3 and P1dB (b) Gain and S_{11} — Plotting (c) Gain and (d) P1dB for variations in R_F	11
2.9 (a) Design of the full chip sent for fabrication in TSMC 65 nm technology node (b) Design of the proposed topology for the Receiver front-end (c)	13
2.10 Block diagram of the full circuit along with the the blocks required for measurement	14
2.11 (a) PCB design for high-frequency Baluns (b) PCB design for low-frequency Baluns, Closed loop buffer BUF602 [18]	15
2.12 Testing setup for Balun Testing with the fabricated PCBs	15
2.13 (a) Output power vs Frequency for NCR2_183_2b (b) Output power vs Frequency depicting cable and substrate losses	16
3.1 Proposed system for Micro-organisms detection	18
3.2 (a) IDE parameters (b) Equivalent model across IDE when placed inside a solution (c) Simulation results of IDE impedance with varying frequency at different widths W	18
3.3 Flow chart of the proposed process for ZnO nanorods growth, with status of the substrate after each step	20
3.4 (a) Basic circuit used for current measurement (b) Proposed circuit for EIS circuit using op-amps	21
3.5 (a) Fabricated IDE (b) FESEM setup (c) Au plated IDE under 10,000X and 25,000X magnification	21
3.6 (a) Elemental analysis output of sample D (b) weight (%) of different elements for different substrate types	22

3.7	(a) Block diagram for AD5933 measurement setup (b) Impedance error from expected mean value of different combinations of RC network	23
3.8	(a) IDE with ZnO nanorods & integrated PCB for impedance measurement (b) experimental setup for the proof-of-concept validation, with the proposed prototype for measurement of yeast concentration (c) change in R_{sol} for different yeast concentrations	24
4.1	Proposed <i>GoldAid</i> Safety System	26
4.2	Architecture of the proposed: (a) Wearable Safety Device (WSD) (b) Base Station Device (BSD) (c) Central Monitoring System (CMS)	27
4.3	(a) Circuit design of the setup (b) Fall testing from heights (>5 m) (c) Same floor fall testing	30
4.4	Plot of acceleration vs time for (a) Falls (b) ADL	32
4.5	Architecture of proposed ML model architecture	33
4.6	Representation of fall on an acceleration vs time plot	34
4.7	(a) Top and bottom view of integrated PCB (b) 3D Printed Enclosure	36
4.8	WSD's OLED depicting different prompts	37
4.9	(a) Range vs TP (b) Energy vs TP for different spreading factor	38
4.10	(a) Map with marked points with the successful transmission (b) Bit error rate (BER) vs Distance plot for Line of Sight (LOS) experiment	40
4.11	Current consumed by i^{th} WSD in one iteration vs Time plot	41
4.12	(a) WSD mounted on the worker's waist and BSD setup at a distance around 200 meters (b) Simulating a fall from an approximate height of 15 meters for testing fall detection algorithm (c) Developed GUI for the central monitoring purposes	42

List of Tables

Table	Page
2.1 Comparison of our proposed RxFE with related works	12
4.1 Summary of data collected	31
4.2 ML model comparison on SisFall data set [54]	32
4.3 Threshold-based fall detection algorithm testing results	39
4.4 Comparison of developed ML model with others [76]	39
4.5 Comparison between two proposed fall detection methods	39
4.6 Comparison of <i>GoldAid</i> with commercial safety devices	43

Chapter 1

Introduction

In recent years, the healthcare sector has witnessed an unprecedented surge in the development and implementation of sensing technologies. These technologies encompass a wide array of devices and sensors that enable continuous and remote tracking of an individual's vital signs, such as heart rate, blood pressure, temperature, oxygen saturation, and more. Moreover, healthcare professionals are increasingly leveraging these advancements to remotely monitor patients, especially those with chronic illnesses or individuals requiring continuous medical attention. Beyond the healthcare sector, sensing technologies have also found significant utility in enhancing industrial safety measures. These advancements have been instrumental in monitoring and ensuring the well-being of workers, particularly in high-risk environments such as manufacturing plants, construction sites, and industrial facilities.

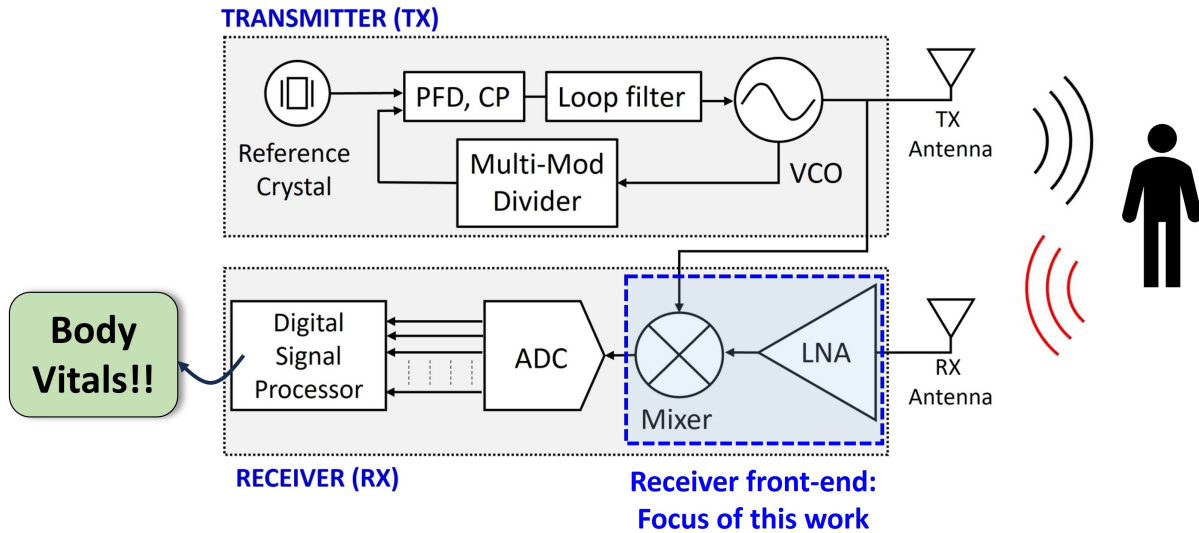


Figure 1.1: High-level architecture of the vital measurement using FMCW radar

Radar technology, particularly Frequency Modulated Continuous wave (FMCW) radar has emerged as a non-contact method for vital sign measurement, detecting subtle movements like chest motions associated with breathing and heartbeats. By continuously emitting and analysing the received radio

frequency signals, FMCW radar's allows for highly accurate monitoring of vital signs. FMCW radar systems often operate within various frequency bands, with some common ranges being 24 GHz and 77 GHz. Figure 1.1 depicts the high-level architecture of vital measurement using FMCW radar. In FMCW radar, the receiver front-end is pivotal for extracting information from reflected signals. It demodulates the received signal, enabling measurement of range and velocity. The front end incorporates signal processing to filter noise and amplify weak signals, ensuring accurate target detection and tracking. Its sensitivity to frequency changes makes it crucial, facilitating the radar's precision in providing reliable object information. In this work, we develop a wide-band receiver front-end based on 4-Path Mixer First approach. The proposed design has been taped out in TSMC 65 nm technology node.

Moreover, addressing the escalating need for portable healthcare and safety solutions, this work presents (1) A portable micro-organism detection system based on Electrochemical impedance spectroscopy (EIS), which can play a pivotal role in diagnosing various strains of pneumonia, emphasizing its imperative function in healthcare diagnostics. (2) An integrated industrial safety system *GoldAid*, which, through sensor integration in an IoT framework, is capable of providing continuous monitoring of workers in large industrial environments.

1.1 Objectives and contributions

The key objective and contributions of the thesis are as follows:

1. 20 GHz RxFE Design and measurement for radar sensing applications
 - (a) Design methodology for a wide-band (8-20 GHz) RxFE has been presented
 - (b) Design and implementation of the proposed 4-Path Receiver in TSMC 65nm technology node is presented
 - (c) Tapeout and measurement of the proposed RxFE is shown
2. Impedance analyser circuits for micro-organisms sensing in healthcare applications
 - (a) Design and testing of electrochemical impedance spectroscopy (EIS) based circuit to calculate impedance of the bio-sensor
 - (b) Measurement results using the fabrication gold-plated ZnO based bio-sensor and the proposed circuit
3. Design and test of an integrated safety system for sensing applications in industries
 - (a) Design methodologies of two fall detection approaches (one for humans, second for machinery) have been discussed
 - (b) Through sensor integration, essential features like vital monitoring, location tracking and SOS alerts has been demonstrated

1.2 Thesis Organisation

Chapter 2 focuses on the design and analysis of a Receiver front-end design using the N-Path Mixer first approach for a frequency of 20 GHz. Extensive efforts has been given to reduce the phase-error for the non-overlapping pulses to get increased linearity. The performance of the designed circuit is confirmed through post-layout simulation results conducted in TSMC 65nm CMOS technology. It also gives an idea about the work done for the tapeout in TSMC 65nm PDK, and focuses on the design of the 20 GHz receiver front-end for fabrication.

Chapter 3 emphasizes on the development of the system for detecting micro-organisms using portable devices. The work focuses on calculating the impedance of a bio-chemical sensor using electrochemical impedance spectroscopy (EIS).

Chapter 4 focuses on the development of a safety system designed especially for industries. It enables rapid medical aid by integrating numerous sensors to detect falls, vitals, live location and other necessary parameters of the industry workers.

Concluding Chapter 5 summarizes the thesis and proposes possible directions for future research. Additionally, it highlights the research contributions from various members within our research group to this thesis.

Chapter 2

Design of a Wideband 8-20 GHz Receiver Front-End with Reduced Local Oscillator Phase-Error in 4-Path Mixer

2.1 Introduction

Modern wireless devices require to support multiple communication protocols, which include frequency ranges from few GHz for Bluetooth/WiFi, to mmWave frequencies for 5G cellular networks. Designing an integrated transceiver capable of accommodating these diverse frequency bands requires wide band receiver front-end (RxFE) architectures. For RxFE, a low-noise amplifier (LNA) typically serves as the first block that interfaces with the antenna, which provides amplification with low-noise and ensures matching with antenna by employing on-chip *LC* components [1]. The frequency-dependent nature of these components poses a significant challenge in achieving front-end tunability. One approach to capture signals across various frequency bands is with the use of multiple narrow-band receiver front-ends tuned at different frequencies. But, this results in more chip area and power consumption, which is undesirable for monolithic systems.

To address the above shortcomings of LNA-First RxFE, passive Mixer-First RxFE architecture has been emerging, particularly RxFE with *N*-path mixers are progressively becoming very popular [2]. Figure 2.1 depicts an *N*-path mixer RxFE, where Radio-frequency (RF) signal is directly applied at the mixer switches and local oscillator (LO) signal is used to control the switches. As shown in Figure 2.1, it requires *N* non-overlapping pulses of LO signal at the mixer with pulse widths of T/N , where *T* is the time period of LO signal. *N*-path mixers have gained popularity due to its numerous advantages. One of them is impedance transparency, which helps in achieving tunable matching at RF port, enabling broadband operation of the front-end [3]. It also provides excellent linearity, as compared to conventional LNA-first approaches, with a slight degradation of noise figure (NF) due to elimination of LNA [2]. Receiver front-end (RxFE) operation with *N*-path mixers at lower frequencies has been extensively evaluated in literature [4, 2]. However, at high frequencies, design of *N*-path mixer based RxFE poses challenges primarily due to: 1) overlap between the LO pulses, which results in charge sharing, leading to reduction in linearity [5, 6] and 2) high input parasitics of the mixer switches present at the RF port,

degrading the tunable matching capabilities of these mixers [7]. In this work, for designing N-path RxFE, operating at high frequencies (>10 GHz), we present 1) design considerations for generating low phase-error non-overlapping LO pulses for improved linearity, 2) design of input matching network under the influence of parasitics dominant at high frequencies, and 3) design and post-layout simulation results of 4-path 8-20 GHz RxFE in TSMC 65 nm CMOS technology to validate the presented considerations.

The outline of the paper is as follows: Section 2.2 gives the background of N-path mixer and its challenges at high frequencies. Section 2.3 presents the proposed architecture, while Section 2.4 discusses about the post-layout simulation results. Finally, Section 3.5 concludes the paper.

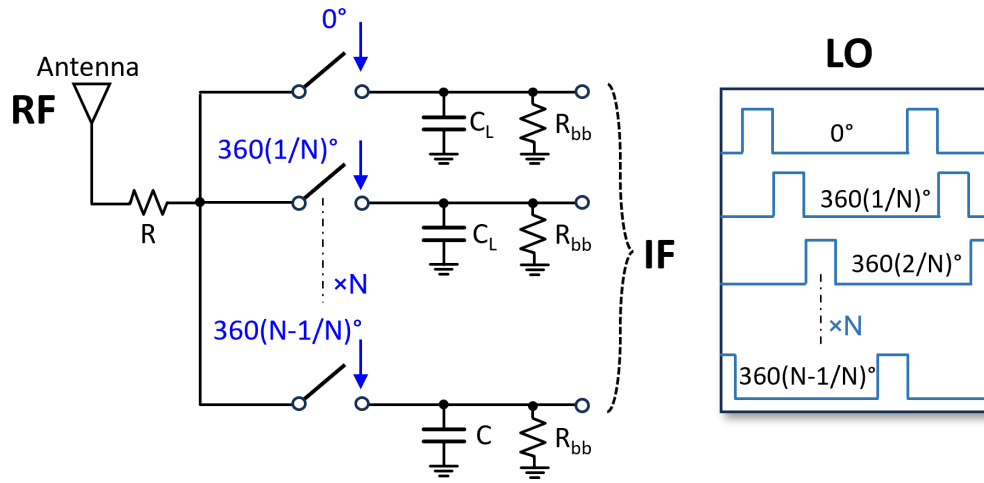


Figure 2.1: Depiction of an N-path mixer based RxFE and its LO phases

2.2 N-path RxFE at High Frequencies : Equivalent Model and Design Challenges

In this section, we discuss the linear time-invariant (LTI) model of N-Path RxFE [3] and present design challenges for high frequency implementation.

2.2.1 Equivalent LTI model of N-Path RxFE

Number of paths in an N-path mixer affects the performance of RxFE. For example, at radio frequencies <6 GHz with higher number of paths ($N=8$), improves its noise figure (NF) and linearity measured in terms of input third order intercept point (IIP3) [8]. However, at for frequencies >10 GHz, higher number of paths such as $N=8$, $N=16$ are not suitable as they increase the parasitic at the RF port resulting into impedance mismatch and reduced linearity. For >10 GHz operations, $N=4$ has been shown a suitable choice in the literature [9, 10, 11]. It is mainly due to the fact that 4-path RxFE reduces the detrimental impact of parasitics, as discussed in the subsequent sub-sections 2.2-B, while providing

adequate NF and IIP3 performance. Moreover, it also relaxes the LO generation requirement as compared to higher path architectures. For these reasons, we have also used a 4-path RxFE architecture in this work. Figure 2.2 depicts the architecture of a 4-path mixer, where each path consists of a load capacitance C_L , and a resistance R_{bb} , depicting the input resistance of the baseband amplifier. An LTI equivalent circuit is shown in Figure 2.3(a). As shown in the figure, input impedance (Z_{in}) at the RF port of the mixer can be calculated as shown in Eq. (2.1),

$$Z_{in} = R_{sw} + (Z_{sh} || \gamma R_{bb}) \quad (2.1)$$

where R_{sw} is the ON resistance of the switch, Z_{sh} is the re-radiation impedance given by (2.2), which represents power losses due to up-conversion of harmonics at RF port [3].

$$Z_{sh} = 4.3(R_{sw} + R_s) \quad (2.2)$$

where R_{sw} , is the mixer switch ON resistance and R_s is the antenna intrinsic impedance. γ is the topology dependent scaling factor, which is given by:

$$\gamma = \frac{\text{sinc}(\frac{\pi}{N})^2}{N} \quad (2.3)$$

where N , is the number of phases. So for $N = 4$, γ is $2/2^2$.

As evident from Eq. (2.1), the real part of Z_{in} can be matched to antenna impedance ($R_s = 50 \Omega$), by regulating R_{bb} . For the circuit shown in Figure 2.2 [3], we used, width of NMOS as $10 \mu\text{m}$, giving $R_{sw}=29 \Omega$, C_L as 500 fF . The R_{bb} is varied from $1 \text{ k}\Omega$ to $100 \text{ k}\Omega$. Figure 2.3(b) depicts this variation of input resistance (R_{in}) seen from the RF port, with varying R_{bb} for 1) LTI equivalent circuit and 2) 4-path mixer. The results from the plot show that, for high values of R_{bb} , simulated R_{in} is unable to follow the input resistance calculated from LTI circuit, which is due to parasitic capacitance of mixer switches present at input RF port [3].

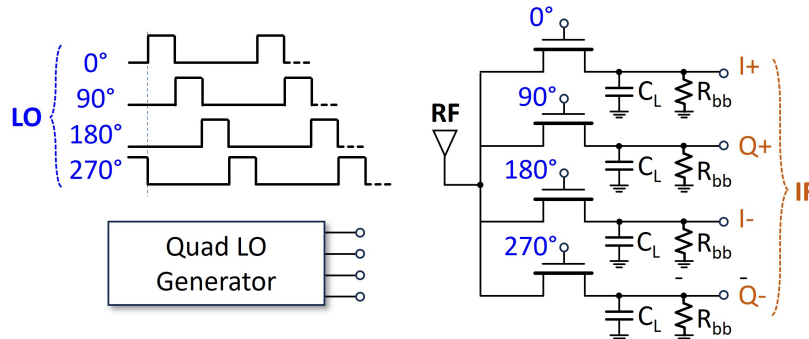


Figure 2.2: Block diagram of 4-path Mixer

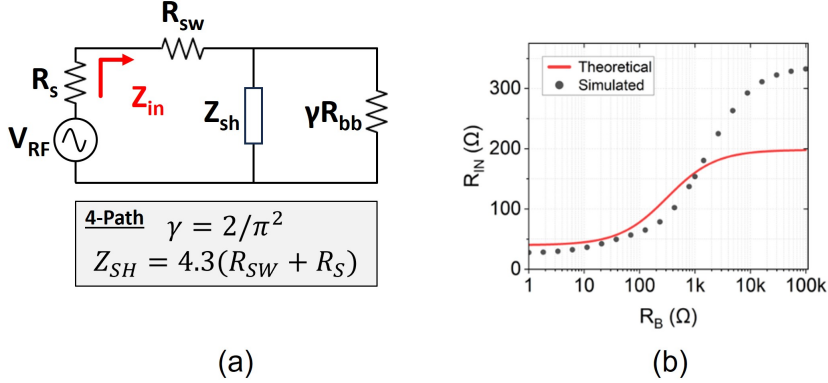


Figure 2.3: (a) LTI equivalent circuit of 4-path Mixer (b) Variation of input resistance with varying R_{BB}

2.2.2 Design Challenges of 4-path RxFE at high frequency (>10 GHz)

2.2.2.0.1 LO phase matching The prerequisite for operation of 4-path mixer is the generation of 25% duty cycle non-overlapping square pulses, which serves as LO signal. When operating at high frequencies, this presents a significant challenge due to the requirement of low rise and fall times, which is in order of few picoseconds for the frequency of around 20 GHz. The common method for generating quadrature non-overlapping pulses is using frequency dividers [12, 13, 14]. In this approach, a signal with frequency $2f_{LO}$, is fed to the dividers to generate f_{LO} , and then the combination of these two signals are used to generate quadrature pulses. The drawback of this approach lies in the need for a signal operating at double the desired LO frequency, along with the requirement for high-power consumption dividers.

2.2.2.0.2 RF input matching Another difficulty faced at high-frequency operation is the input parasitics of the mixer switches. The LTI equivalent circuit shown in Figure 2.3(a) is valid for low operating frequencies, which omits the input parasitic capacitance (C_{par}) for simplicity. The increased effect of parasitic capacitance at high-frequencies lowers the effective shunt impedance Z_{sh} , which increases the power losses due to the up-conversion at RF port. This degrades the linearity of the mixer [6]. To reduce these parasitic capacitances, smaller size of mixer switches should be considered. However, this will increase switch ON resistance (R_{sw}), which should be ideally as low as possible. To achieve an optimal design, the size of the mixer switches should be carefully chosen to strike a balance between R_{sw} and C_{par} . The size of switch also tends to have an effect on the noise figure (NF) of the receiver, which is defined in [3] as:

$$NF = 1 + \frac{R_{sw}}{R_s} + \frac{(R_s + R_{sw})^2(1 - 4\gamma)}{4\gamma R_s R_{sw}} \quad (2.4)$$

In this equation, the baseband resistance is neglected. To minimize NF, R_{sw} is calculated as:

$$R_{sw} = R_s \sqrt{1 - 4\gamma} \quad (2.5)$$

Using the above equation, the size of the mixer switch can be decided. The implementation of the full receiver is given in the next section.

2.3 Design consideration and implementation of wideband 4-path RxFE

2.3.1 LO Generation

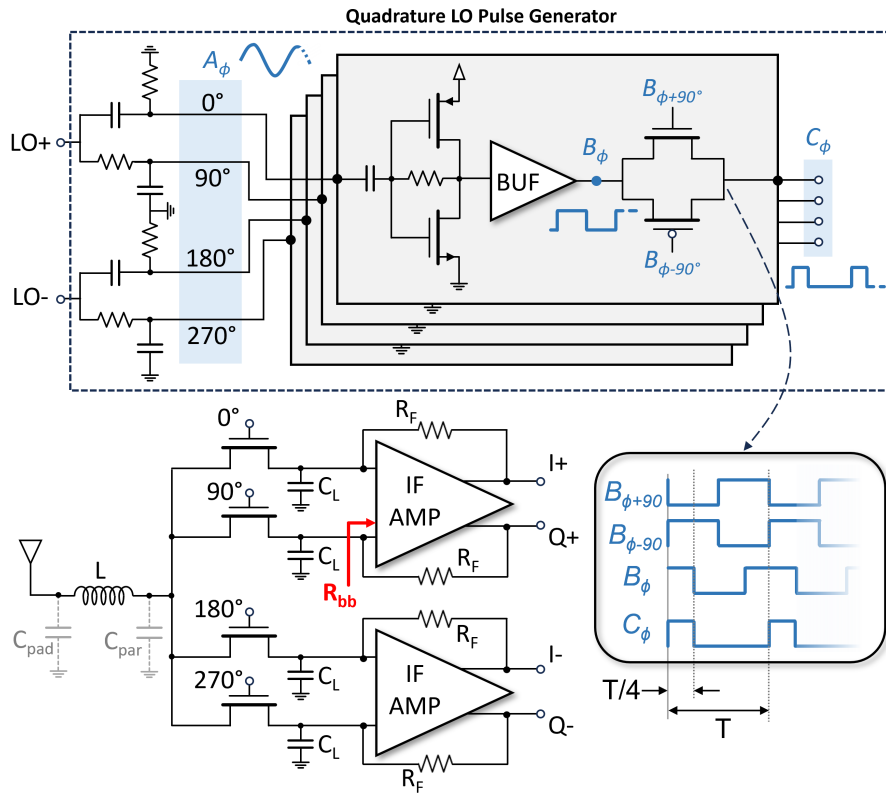


Figure 2.4: Block diagram of full Receiver front-end

In Figure 2.4, the generation method of quadrature non-overlapping LO pulses is depicted, which serve as inputs to the drive the gates of the mixer switches. At operational frequency of 20 GHz, the pulse width of these LO signals measures 12.5 ps. Notably, the rise and fall time should be shorter than half of the pulse width, which is 6 ps in this case. The input to the LO generator is a differential sinusoidal signal with frequency f_{LO} , which is input to the RC phase shifter network (at node $LO+$ and $LO-$). The two pair of high-pass filter and low-pass filter network realises quadrature sinusoidal signals (at node A) with relative phase shifts of 0, 90, 180 and 270 degrees. These signals are then fed to the buffer network, which converts these sinusoidal quadrature signal to 50% duty cycle square (pseudo-sinusoidal) pulses (at node B). The AND logic implementation for generating 25% non-overlapping pulses in implemented from transmission gates (at node C). If the input of transmission gate is consid-

ered B_ϕ , then the control signal for NMOS and PMOS are $\pm 90^\circ$ phase-shifted signals i.e. $B_{\phi+90}$ and $B_{\phi-90}$ respectively. The input power given to the LO signal is around 10 dBm to cover for the losses in the passive network. The buffer are designed to drive three nodes, one is input of a transmission gate, and other two are gate of the switches. Careful consideration should be given to the parasitics and input capacitances all the nodes, while designing buffers in order to maximize the swing and effectively balance the trade-off between power consumption and performance. The proposed circuit achieves quadrature pulse generation from a frequency of 8–20 GHz with a current consumption of around 40 mA at 1.2 volts power supply. As shown in Figure 2.5(a), quadrature error of less than 7 for all process corners is achieved. The rise and fall times of <5 ps are achieved for a LO frequency (f_{LO}) of 20 GHz, as confirmed from transient simulation results shown in Figure 2.5(b).

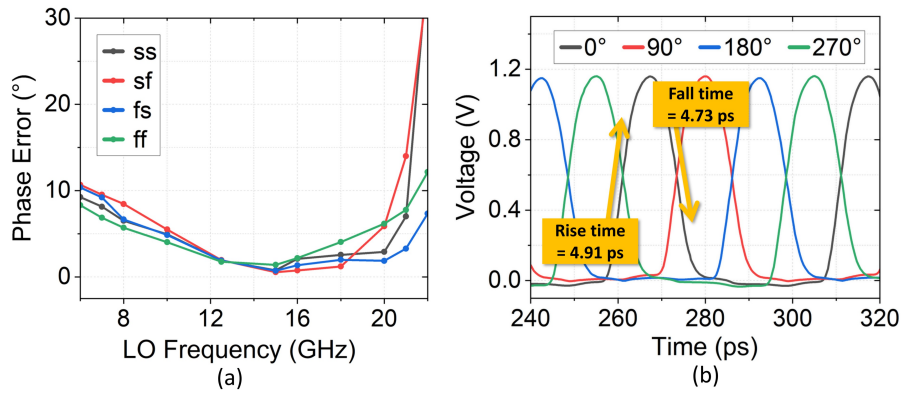


Figure 2.5: (a) Quadrature error vs LO frequency (b) Transient plot of Quadrature LO pulses

2.3.2 Matching network design for 4-path mixer

To minimize the loss and maximize the power transfer from antenna to the front-end, the intrinsic impedance of the antenna must be matched with the input impedance seen at the RF port. Impedance transparency property of N-Path mixers enables straight-forward matching for low-frequency operation by tuning the baseband feedback resistor R_F as explained in Section 2.2.

As shown in Figure 2.4, when operating at higher frequencies, the parasitic capacitance (C_{par}) of the mixer switches becomes prominent. This addition of capacitance degrades the input match as explained in Section 2.2. So for more precise matching a series input inductor is added, forming a π network with pad capacitance (C_{pad}) and parasitic capacitance (C_{par}). Figure 2.6(a) depicts integrated matching network with LTI equivalent circuit of 4-path mixer. Figure 2.6(b). plots the S_{11} value at RF source port by varying R_{bb} . For this simulation the LO frequency is set to 20 GHz, using the proposed LO generator depicted in Figure 2.4. The sharp decline in S_{11} validates the impedance transparency and its use in matching the antenna impedance at the RF port.

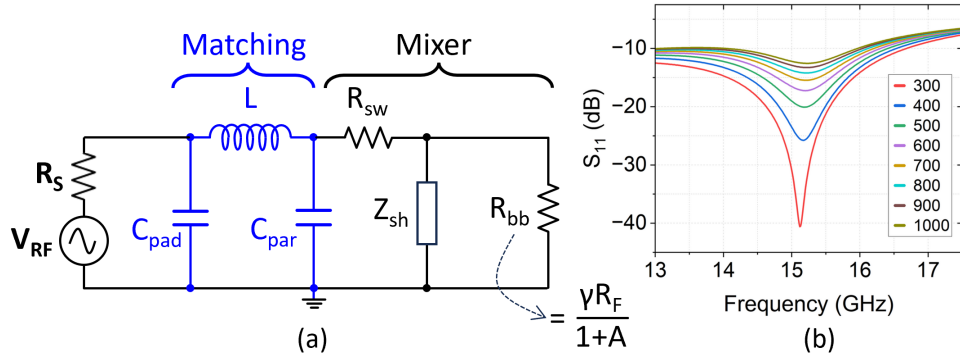


Figure 2.6: (a) LTI equivalent circuit of 4-path Mixer with matching network (b) Plot of S_{11} vs Frequency for different R_{bb} values

From the design challenges discussed in Section 2.2-B and from Eq. 2.5, the R_{sw} value calculated as 21.9 . To achieve this, mixer switches are implemented using 20 μm wide NMOS switches, giving the average simulated R_{sw} value of ≈ 20 .

2.3.3 IF Amplifier

Figure 2.7(a) depicts the implemented baseband amplifier with a fully-differential operational transconductance amplifier (OTA) A_1 as a trans-impedance stage (TIA). The differential inputs from the I and Q paths are fed into an NMOS differential pair with PMOS active loads. A CMFB network, consisting of resistors R_{CM} and a single-ended single-stage OTA A_2 , is employed to maintain a constant common-mode voltage (V_{OCM}) at the output. The equal current densities in both amplifiers help reduce systematic offset issues. Feedback resistors R_F can be tuned to program the gain and the input impedance of the TIA. This input impedance can be denoted by R_{bb} , whose relation to R_F can be defined as [15]:

$$R_{bb} = \frac{1}{g_m} + \frac{R_F}{g_m r_o} \quad (2.6)$$

where g_m is trans-conductance of OTA, r_o is output resistance. R_F , can be varied to control the impedance seen at RF port R_{bb} , which is matched to antenna using π matching network. As shown in Figure 2.4, mixer outputs are directly coupled to the IF amplifier inputs. The CM voltage at input of IF amplifier is set, according to the output CM voltage due to feedback resistance R_F . For keeping both these voltage level near to 0, it became necessary for the use of dual voltage power supply (± 600 mV). The simulated open loop gain of the designed OTA A_1 is 25 dB, with a gain-bandwidth of 30 MHz.

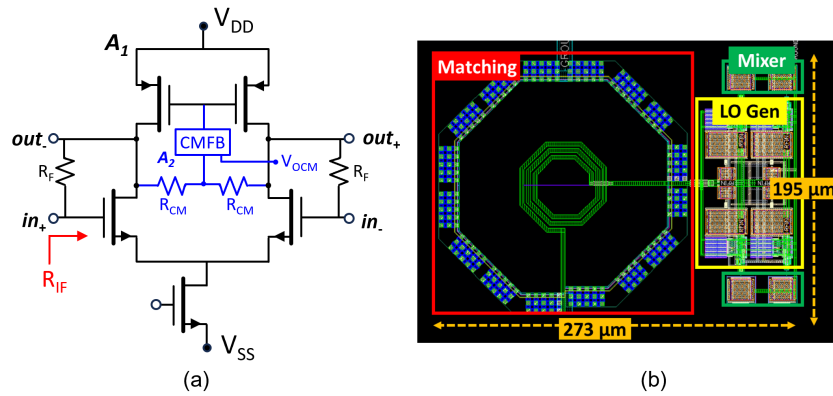


Figure 2.7: (a) Fully differential OTA used as IF amplifier in TIA configuration (b) Layout of the proposed receiver front-end in TSMC 65nm

2.4 Simulation Results

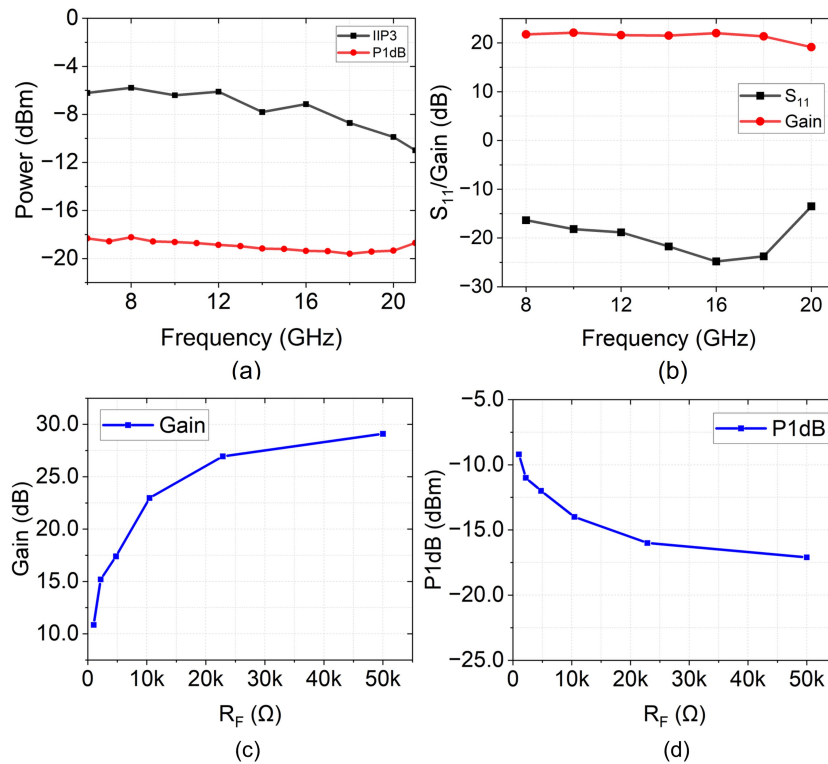


Figure 2.8: Plot by varying frequency for (a) IIP3 and P1dB (b) Gain and S_{11} — Plotting (c) Gain and (d) P1dB for variations in R_F

Figure 2.7(b) shows the layout of the receiver front-end chain, designed in TSMC 65nm technology node. The total area of LO generation and matching circuit is $195 \mu\text{m} \times 273 \mu\text{m}$. The receiver gives reliable performance for frequency range of 8 GHz to 20 GHz, while consuming a total power-consumption of 66 mW at 1.2 volts supply. Figure 2.8(a) exhibits the post-layout simulated IIP3 and P1dB vs the LO frequency. For IIP3, a two-tone test, with signal frequencies $f_{LO} + 10 \text{ MHz}$ and $f_{LO} + 11 \text{ MHz}$ were used, making the third inter-modulation (IM3) component fall at 9 MHz. Figure 2.8(b) illustrate the impedance matching by plotting the S_{11} , for different LO frequencies. This plot confirms the tuning capabilities of the proposed matching network for 4-path receivers. Figure 2.8 illustrates the variation of gain and P1dB, with varying baseband feedback resistor R_F . As seen from the plot in Figure 2.8(c), increasing R_F , increases the gain. This causes a limit on input signal which can be given to IF amplifier, which in turn causes reduction in linearity, as depicted from P1dB plot in Figure 2.8(d).

Table 2.1: Comparison of our proposed RxFE with related works

	[9] RFIC (2016)	[16] ISSCC (2018)	[17] JSSC (2020)	[13] ESSCIRC (2021)	This Work
Frequency [GHz]	20 \rightarrow 30	27 \rightarrow 29.75	24.5 \rightarrow 43.5	4 \rightarrow 31	8 \rightarrow 20
Results	Measured	Measured	Measured	Measured	Simulated
Tech. Node	45 nm	65 nm	45 nm	45 nm	65 nm
Topology	MF Direct	LNA first	Low-IF RX	LNA first	4-path MF
NF [dB]	8 \rightarrow 10.4	5.7	3.2 \rightarrow 6.1	5.2 \rightarrow 9.8	12.88
P1dB [dBm]	-13 \rightarrow -9.3	-30	-7 \rightarrow -25	-17	-9.2 \rightarrow -17.1
IIP3 [dBm]	-9.7 \rightarrow -2.3	-	-	-6.6	-8 \rightarrow -12.2
Gain [dB]	8.9 \rightarrow 20.6	33	35.2	17 \rightarrow 28	10 \rightarrow 29
Power [mW]	41	52.5	60	178 \rightarrow 318	66
@VDD [V]	@0.9 & 1.8	@1.1	@1	@0.6 \rightarrow 1.2	@1.2
Area [mm²]	0.75	0.46	0.66	1.95 [#]	0.0532*

* Area of IF amplifier is not included, # Die size, MF: Mixer-First

Table 4.4 shows the summary and comparison with the other works. As shown in Table 4.4, the considerations presented in this work help in achieving improved linearity over a wider frequency range while consuming much smaller area.

2.5 Conclusion

In this work, design of a 4-path mixer based 8–20 GHz RxFE with programmable gain of 10 to 29 dB has been presented. To achieve this, considerations for the faithful generation of different non-overlapping phases of LO with wide band RF input matching is also presented. Design and post-layout simulation results of a 4-path mixer based 8-20 GHz RxFE with programmable gain of 10 to 29 dB in TSMC 65 nm CMOS technology is also presented in this work. Post-layout simulations show that, the proposed design achieves an IIP3 of > -10 dB, S_{11} of < -12 dB and consumes total power of 66 mW from 1.2 V supply.

2.6 Measurement circuit for the proposed topology in TSMC 65 nm technology node

This section provides a concise overview of the designed circuit of the proposed receiver front-end for fabrication. The design has been sent for fabrication in TSMC 65 nm technology node in conjunction with various other circuits required to build the FMCW transceiver chip.

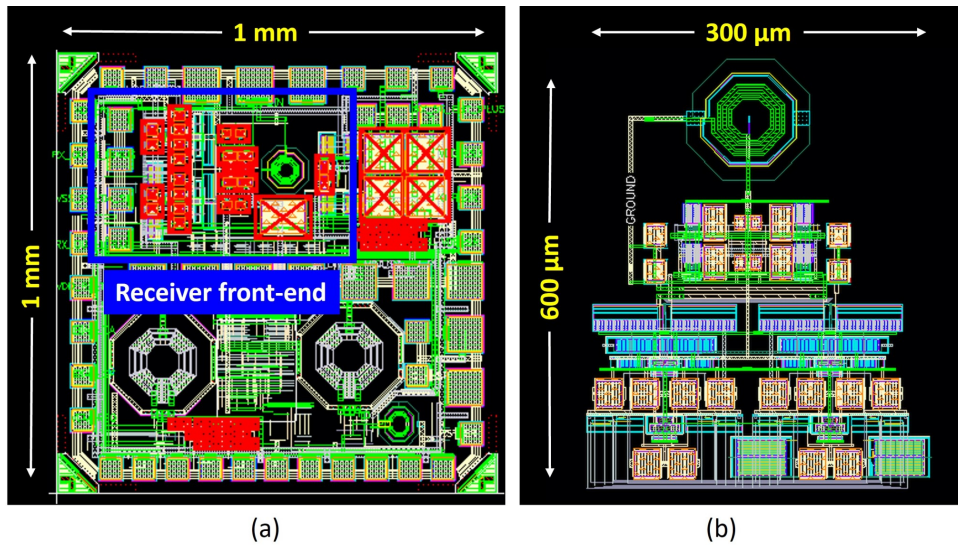


Figure 2.9: (a) Design of the full chip sent for fabrication in TSMC 65 nm technology node (b) Design of the proposed topology for the Receiver front-end (c)

Figure 2.9(a) illustrates the full layout of the 1mm×1mm chip, which is sent for fabrication. It consists of various major designs of the FMCW transceiver chip which includes a Voltage-controlled oscillator, Divide by 512 frequency divider, Delta-Sigma Modulators by Pranjali Mahajan, High-Pass filter for baseband stage, Shift-register & other peripheral circuits. Figure 2.9(b) depicts my major

contribution, which is the design of the proposed 8-20 GHz 4-Path Mixer-first Receiver front-end. Apart from this, I have contributed to the pad frame’s design and the full chip’s high-level routing. The padframe consists of strategically placed 50 pins, which allows the designer to test all the circuits.

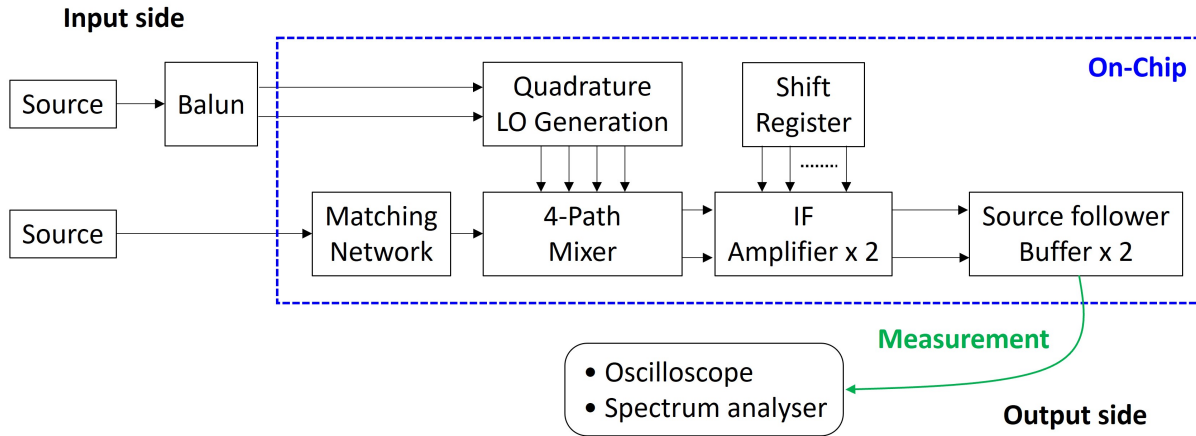


Figure 2.10: Block diagram of the full circuit along with the the blocks required for measurement

Figure 2.10 illustrates the architecture of the proposed circuit, along with additional blocks required for testing. The output of the last stage, i.e. the IF amplifier, is fed to the source follower stage to drive the 50 Ω load of the spectrum analyser. The source follower has different power lines to measure the power of the RxFE and additional circuitry separately. As the proposed circuit consists of two sets of tunable resistors, the control pins require a digital input. This input is controlled by a 48-bit shift register present on the chip. The input of the shift register, i.e. input, clock and reset pins can be controlled by an external FPGA or a microcontroller. To verify the DC voltage on the control pins of the tunable resistors, the MSB or the last bit of the shift register is taken out through a buffer for external measurement.

Figure 2.10 depicts the testing setup for measuring the proposed circuit on the chip. As shown in Figure, different set of instruments will be used for measurements, such as:

- Vector Network analyser for S-parameter analysis
- Spectrum analyser for measuring parameters like IIP3, P1dB, conversion gain, etc
- Oscilloscope for analysing transient waveforms

As seen from Figure 2.10, an off-chip balun is required to convert the single-ended sinusoid signal to a differential signal. To achieve this, different sets of balun are under testing. Figure 2.11 depicts the EAGLE design of some of the testing boards which have been fabricated. Also, at high-frequencies, the losses from RF cables, connectors and the PCB substrate should be accounted for; therefore, all these things are being characterised using the fabricated PCBs.

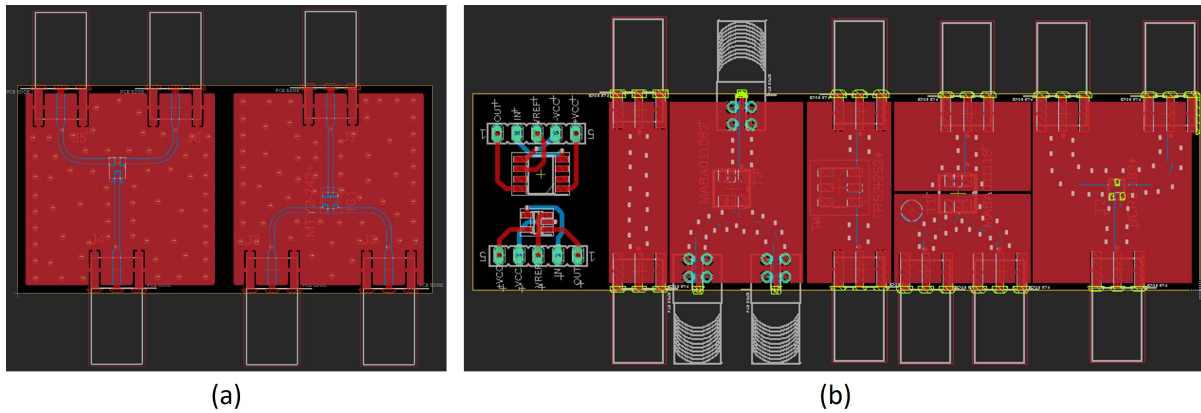


Figure 2.11: (a) PCB design for high-frequency Baluns (b) PCB design for low-frequency Baluns, Closed loop buffer BUF602 [18]

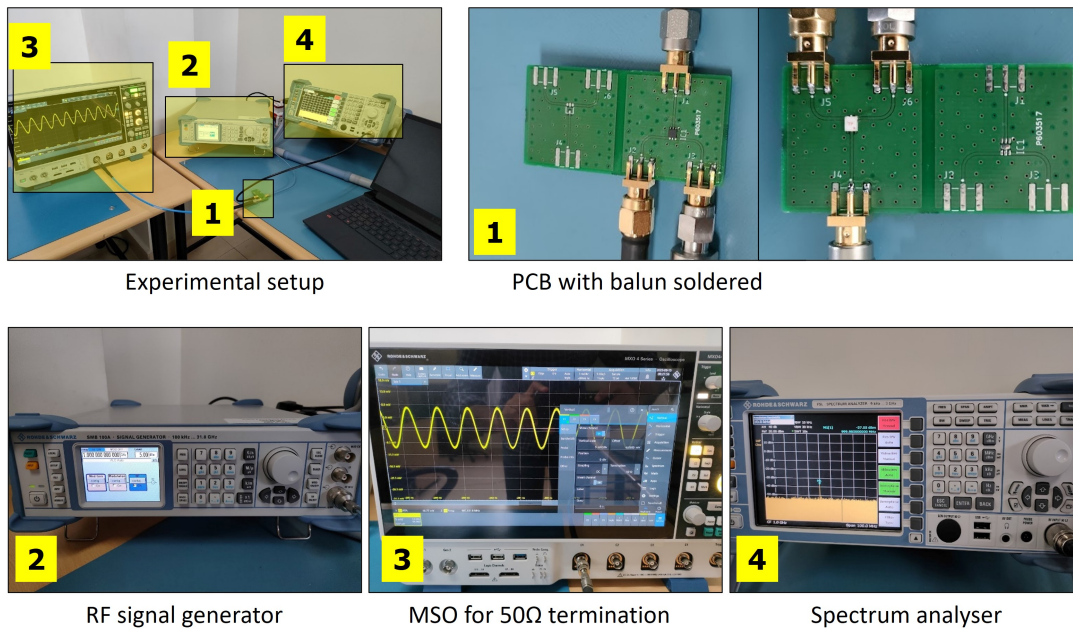


Figure 2.12: Testing setup for Balun Testing with the fabricated PCBs

The PCB are designed with impedance control; all the signal traces are tuned at a particular frequency. The trace width is then calculated using a tool named "TXLINE" from National Instruments. Figure 2.12 depicts the testing setup with the fabricated PCBs. Figure 2.13 presents the results for some of the test cases performed on the fabricated PCBs. For instance, Figure 2.11(a) plots the output power vs the frequency for an input power of 5 dBm for the Balun NCR2_183_2b [19].

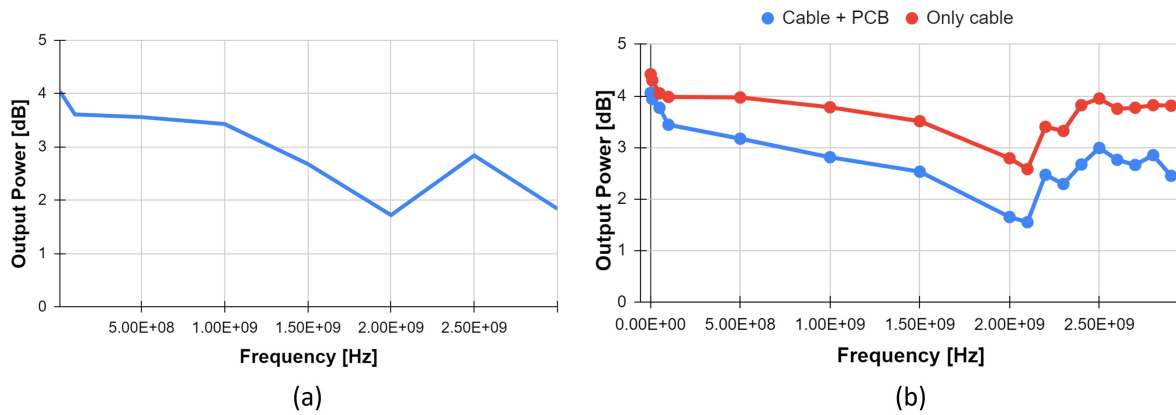


Figure 2.13: (a) Output power vs Frequency for NCR2_183_2b (b) Output power vs Frequency depicting cable and substrate losses

This brings us to the end of this chapter, where we discussed the Receiver front-end circuit developed for FWCW radar. It will be further used to develop the full FMCW transceiver chip, which can be used in various applications. The next chapter discusses the design of the systems that will be used to improve the diagnosis of microorganisms using a portable device based on electrochemical impedance spectroscopy (EIS).

Chapter 3

Design of Integrated System for Detection of Micro-organisms with Fabrication and Testing of ZnO Nanorods based Biosensor

3.1 Introduction

Micro-organism detection plays a vital role in safeguarding human well being, environmental integrity and industrial efficiency. In the absence of suitable detection techniques, a range of detrimental outcomes can arise, including delayed diagnosis and treatment of diseases. Therefore the presence of appropriate detection techniques is crucial to guarantee timely and precise identification. Impedance spectroscopy is a powerful technique that has gained significant attention in various scientific fields due to its ability to monitor and analyze electrical properties of biological samples [20, 21, 22, 23].

A. Soley et al. conducted a study focusing on yeast growth monitoring through impedance spectroscopy [20] using a Hewlett Packard 4192A impedance analyzer connected to a computer. However, lack of portability restricts its potential applications in biomedical sensing. Borgohain [21] proposed a biosensor utilizing resistance measurement-based circuit to differentiate between gram-positive and gram-negative bacteria. However, the circuit's susceptibility to errors necessitates further development for enhanced accuracy. T. Houssin presented a non-invasive method for detecting polluting parasites specifically *Cryptosporidium parvum*, in water [22]. Their study employed the Agilent 4294A impedance analyzer for impedance spectroscopy. However, to facilitate outdoor applications, there is a growing need for improved portable systems. D.K. Kamat developed a bioimpedance system for skin monitoring, utilizing the AD5933 [23] and Ag/AgCl electrodes for impedance spectroscopy. While this approach yielded promising results, the high cost of the electrodes raises concerns regarding affordability and scalability. These challenges related to portability, accuracy, and cost-effectiveness need to be addressed to maximize the utility of these techniques.

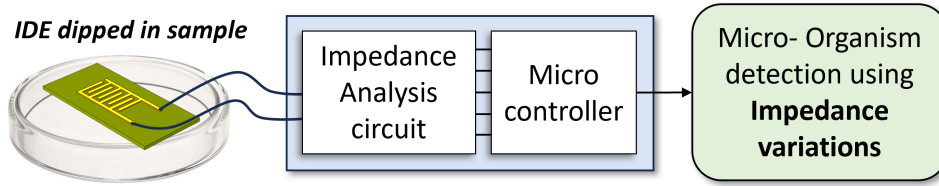


Figure 3.1: Proposed system for Micro-organisms detection

To address the above mentioned challenges, this research presents 1) Zinc Oxide (ZnO) nanorods based cost-effective, portable integrated system for micro-organism detection, which is based on electrochemical impedance spectroscopy (EIS), 2) considerations and methodology for the fabrication of ZnO nanorods with high-yield, 3) experimental results through scanning electron microscope to validate the efficacy of the proposed methods, and 4) measurement results of the proposed system prototype for detection of a micro-organism (yeast) to demonstrate the utility and effectiveness of the proposed methods and system. ZnO nanorods are chosen for their biocompatibility, strong chemical/thermal stability, and adjustable properties through size control [24, 25]. The outline of the paper is as follows: Section 3.2 introduces the proposed sensor and interface circuit, Section 3.3 presents the design considerations for biosensor and interface circuit, Section 3.4 outlines the sensor fabrication method and the implementation of the impedance measurement circuit. Finally, the paper concludes with Section 3.5.

3.2 Proposed sensor and interface-circuit for micro-organism detection

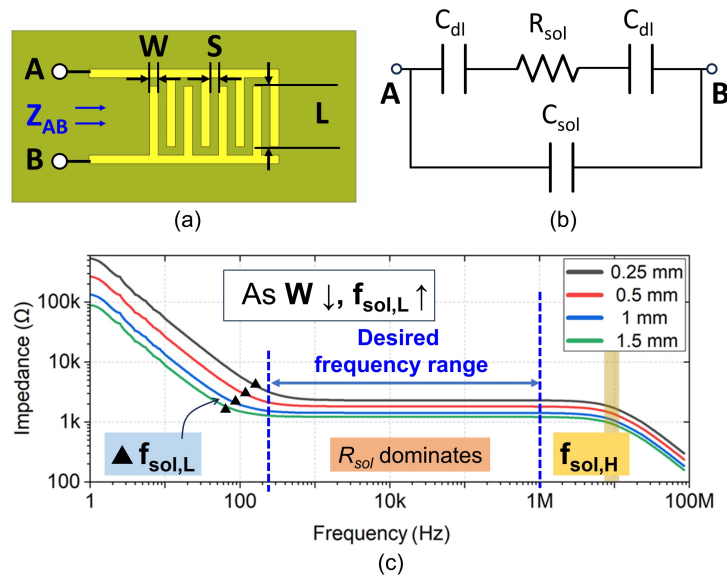


Figure 3.2: (a) IDE parameters (b) Equivalent model across IDE when placed inside a solution (c) Simulation results of IDE impedance with varying frequency at different widths W

Figure 3.2 shows the geometry of an interdigitated electrode (IDE) for the proposed sensor. As shown in the figure, IDE has 8 fingers, each finger width (W) is 1 mm, the spacing (S) between fingers is 1 mm, and the length (L) is 4 mm. Figure 3.2(b) shows the equivalent model of the unprocessed IDE when it is immersed in a solution, where R_{sol} , C_{sol} , and C_{dl} are the solution-resistance, solution-capacitance and capacitance of the double layer (electrode surface and solution) in IDE, respectively [26, 27, 28]. Values of R_{sol} , C_{sol} , and C_{dl} depends on the dimensions of the IDE. R_{sol} and C_{sol} can be described by Eq. (3.1) and Eq. (3.2), respectively [26, 27, 28]

$$R_{sol} = \frac{K_{cell}}{\sigma_{sol}} \quad (3.1)$$

$$C_{sol} = \frac{\epsilon_0 \epsilon_{rsol}}{K_{cell}} \quad (3.2)$$

where σ_{sol} and ϵ_{rsol} are conductivity and relative permittivity of solution, respectively. K_{cell} is used to mathematically depict the influence of IDE dimensions on each component of the equivalent model and is given by Eq. (3.3).

$$K_{cell} = \frac{2}{(N-1)L} \times \frac{K(k)}{K(\sqrt{1-k^2})} \quad (3.3)$$

where, $K(k)$ and k are as given by Eq. (3.4) and Eq. (3.5), respectively.

$$K(k) = \int_0^1 \frac{1}{\sqrt{(1-t^2)(1-k^2t^2)}} dt \quad (3.4)$$

$$k = \cos\left(\frac{\pi}{2} \times \frac{W}{S+W}\right) \quad (3.5)$$

As shown in Figure 3.2(b), C_{dl} for planer electrodes can be approximated to be directly proportional to the Stern layer characteristic capacitance, which is around 10-20 $\mu\text{F}/\text{cm}^2$ [29]. Since C_{dl} is the capacitance caused by the accumulation of ions at electrodes, it depends on the electrode area in contact with the solution and given by Eq. (3.6).

$$C_{dl} = 0.5 \times W \times N \times L \times C_{stern,surface} \quad (3.6)$$

As shown in Figure 3.2(a) and Figure 3.2(b) Impedance (Z_{AB}) across IDE terminals A and B varies with frequency. Figure 3.2(c) shows magnitude of Z_{AB} with respect to frequency for different values of W when IDE is kept in water (average σ_{sol} of water = 50 mS/m^2 and $\epsilon_{rsol} = 80\epsilon_0$)[29]. As shown in Figure 3.2(c), the constant $|Z_{AB}|$ region in the frequency range of 100 Hz to 1 MHz is mainly due to R_{sol} as discussed in [26, 27]. The expected resistance of the solution (water) from Figure 3.2(c) falls within the range of 1 - 3.5 $\text{k}\Omega$. R_{sol} varies with presence of different concentrations of micro-organisms[21, 26]. This variation can be measured through electrochemical impedance spectroscopy (EIS), which involves sweeping an AC voltage of different frequencies and observing the change in the impedance. Figure 3.2(c) also shows that reducing the finger width (W) increases the lower dominant frequency ($f_{sol,L}$) of R_{sol} , while there is no significant effect on higher dominant frequency ($f_{sol,H}$). To

ensure flexibility in selecting the frequency range for measuring solution resistance, it is desirable for R_{sol} to dominate across a wide frequency range. This dominance allows for the choice of an optimal frequency range to accurately measure and analyze solution resistance, which is crucial for detecting variations in yeast concentration.

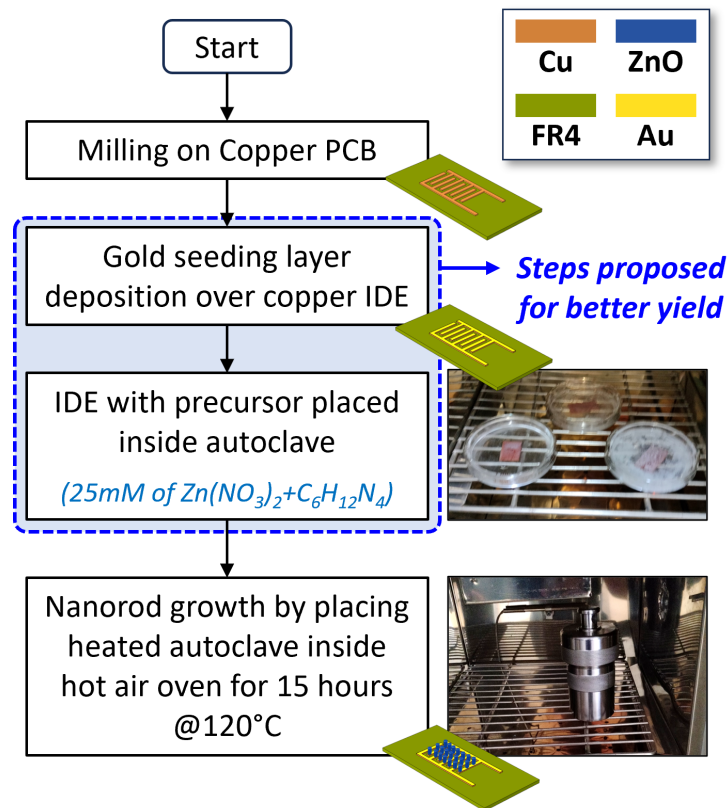


Figure 3.3: Flow chart of the proposed process for ZnO nanorods growth, with status of the substrate after each step

3.3 Considerations for EIS Circuit Design

The generic process for ZnO nanorods growth involves the deposition of a ZnO seed layer on a substrate through dip coating, followed by heating at high temperatures with the precursor solution for about 6 hours [21]. For higher yield of ZnO nanorods, it is required to have a seed layer with high number of nucleation sites, to facilitate the formation of well-defined crystalline structures. For this gold has proven to be a suitable choice as the seed layer [30]. As shown in [31] [32], borosilicate glass substrate with pure gold deposited thinfilm at very high temperature ($>400^{\circ}\text{C}$) can be used to form the gold seed layer. However, this increase the cost of IDE drastically.

Therefore, as shown in Figure 3.3, for developing cost-effective IDEs at large scale, we propose empirically developed fabrication steps to improve the ZnO nanorods yield on a low-cost FR4 substrate. In this process, pure gold IDEs are replaced with low-cost FR4 substrate, where Copper (Cu) IDE can be electroplated with gold, substantially reducing the cost. Moreover, as shown in Figure 3.3, we also propose to use 120°C temperature, 15 hours of processing time with an autoclave as FR4 substrate can only handle <170°C [33].

3.3.1 EIS circuit design consideration

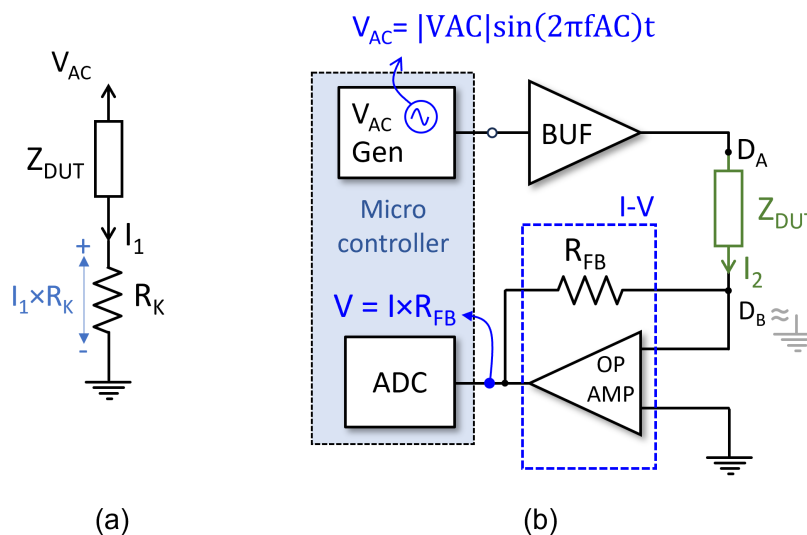


Figure 3.4: (a) Basic circuit used for current measurement (b) Proposed circuit for EIS circuit using op-amps

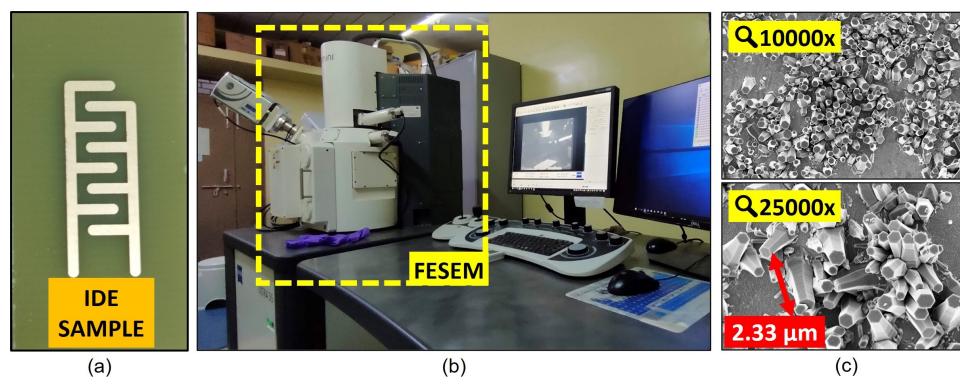


Figure 3.5: (a) Fabricated IDE (b) FESEM setup (c) Au plated IDE under 10,000X and 25,000X magnification

Figure 3.4(a) depicts the general principle of impedance (Z_{DUT}) measurement of a DUT, where voltage (V_{AC}) is applied and AC current (I_1) is measured by computing voltage across resistor (R_K), which is added in series with DUT. As discussed in Section 3.2, the magnitude variation of impedance is in the range of a few k for the desired micro-organism i.e. yeast. Figure 3.4(b) shows the impedance measurement approach used in this work, where an op-amp based I-V converter is employed to measure the current flowing through DUT [34]. With this method, DUT node D_B acts as virtual ground. The gain of the I-V converter is determined by an external feedback resistor R_{FB} as shown in the figure. To get the best sensitivity and prevent saturation of I-V converter output voltage, R_{FB} value is set to the expected value of the DUT impedance estimated from the equivalent model discussed in Section 3.2. As shown in Figure 3.4(b), the range of applied frequency (f_{AC}) is decided with the help of 3.2(c), where R_{sol} dominates.

3.4 Implementation details and Measurement results

3.4.1 Sensor Fabrication and SEM results

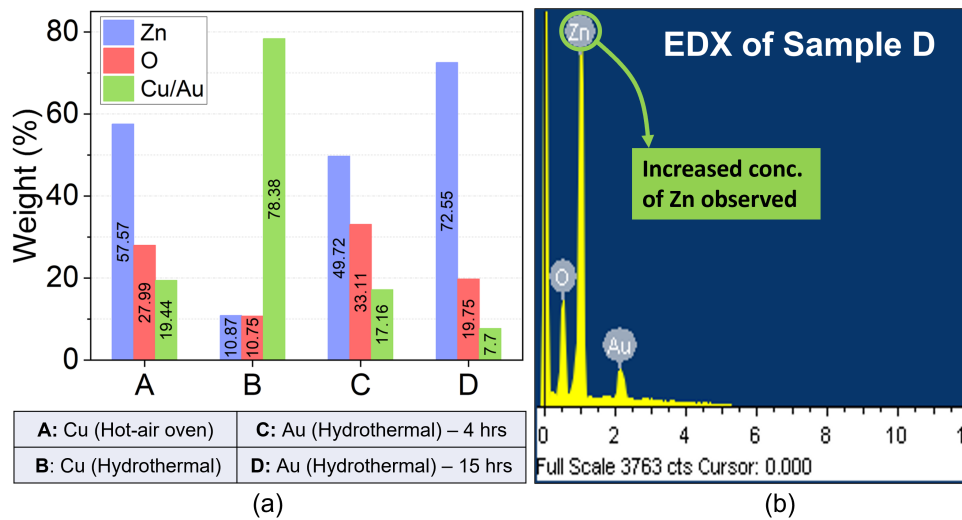


Figure 3.6: (a) Elemental analysis output of sample D (b) weight (%) of different elements for different substrate types

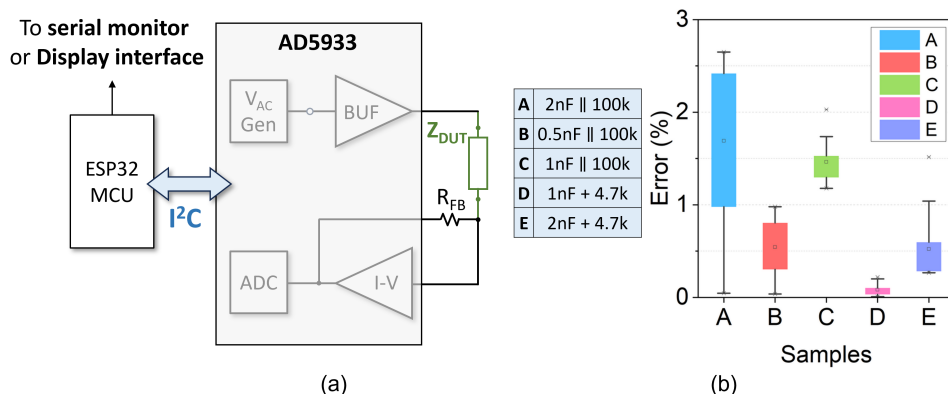


Figure 3.7: (a) Block diagram for AD5933 measurement setup (b) Impedance error from expected mean value of different combinations of RC network

Figure 3.5(a) shows the fabricated gold-coated IDE with ZnO nanorods following process mentioned in Section 3.3A. For this, 25 mM equi-molar solution of zinc nitrate hexahydrate $[\text{Zn}(\text{NO}_3)_2 \cdot 6\text{H}_2\text{O}]$ and hexamine $[\text{C}_6\text{H}_{12}\text{N}_6]$ is taken as precursor solution[21]. Then IDE and the precursor solution are kept inside Polytetrafluoroethylene (PTFE) lined hydrothermal reactor and placed inside an oven at 120°C for 15 hours. After the process, the substrate is cleaned with deionised water and dried at 120°C for 1 hour. As shown in Figure 3.5(b), scanning electron microscopy (SEM) is conducted to examine nanorods formation by using Zeiss Field Emission Scanning Electron Microscope (FESEM). Figure 3.5(c) displays FESEM images of the gold IDE at magnifications of 10,000X and 25,000X. These images demonstrate successful ZnO nanorods growth across the IDE surface, with the distinctive hexagonal crystalline structure characteristic of ZnO nanorods formation when utilizing zinc nitrate and hexamine as precursors validating the process described in Figure 3.3 [35].

For developing the empirical process, 4 IDE samples A-D, were fabricated. Sample A is fabricated using Cu IDE using dip coating process for seed layer and hot air oven at 120°C for 15 hours. Sample B, C are fabricated on Cu (dip coating for seed layer) and Au plated IDE respectively using autoclave and heated at 120°C for 4 hours. Sample D is fabricated on Au plated IDE using autoclave and heated at 120°C for 15 hours. Figure 3.6(a) illustrates a comparative analysis of four different procedures based on the elemental analysis results through energy-dispersive X-ray spectroscopy (EDX) feature of FESEM. Comparison shows that using Cu as the IDE material and dip coating a ZnO seed layer resulted in a lower weight percentage of ZnO nanorods, as initially proposed. The average increase in ZnO weight (%) from sample A, B (with dip coat) to sample C (with Au layer) is 29.24%. Moreover, longer heating duration inside the hydrothermal reactor led to a 9.47% increase in ZnO weight (%) (from sample C to D) and 92.3% of overall ZnO nanorods weight (%) on sample D. Figure 3.6(b) displays the elemental analysis results of sample D, where a higher number of Zn and O peaks are observed compared to Au, indicating a more significant formation of ZnO nanorods.

3.4.2 EIS implementation and Characterization

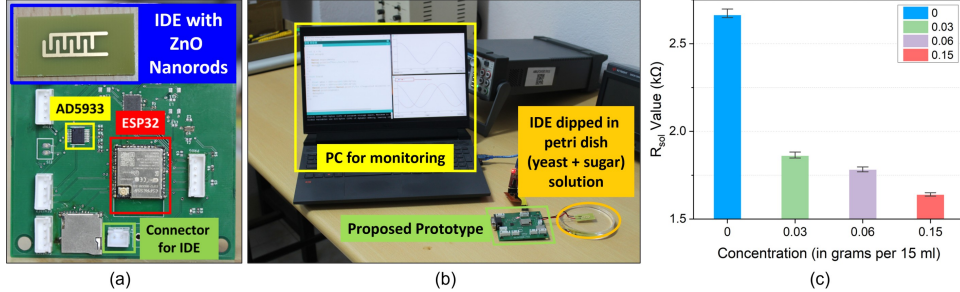


Figure 3.8: (a) IDE with ZnO nanorods & integrated PCB for impedance measurement (b) experimental setup for the proof-of-concept validation, with the proposed prototype for measurement of yeast concentration (c) change in R_{sol} for different yeast concentrations

As shown in Figure 3.7(a), to implement the EIS circuit, we employed an AD5933 impedance analyzer IC, which is capable of measuring impedance values within the range of 1 k to 10 M across a frequency range of 1 Hz to 100 kHz[30]. The simulation results depicted in Figure 3.2(c) indicate that the frequency range supported by the AD5933 IC aligns with the dominant frequency range of the solution resistance (R_{sol}) that we intend to observe. To assess the measurement accuracy, the AD5933 was initially tested using a combination of RC networks to observe any deviations from the taken calibration value. Figure 3.7(b) illustrates the error deviation $<2.5\%$ from the expected mean impedance values obtained during these tests. For measuring the IDE solution resistance (R_{sol}), the AD5933 was calibrated using a 3.3 k resistor, as the expected resistance of R_{sol} based on the performed simulations ranged between 1 k and 3.5 k.

3.4.3 System prototype

The proposed prototype in Figure 3.8(a) integrates the ZnO nanorods sensor shown in Section 3.4A with AD5933. A micro-controller (ESP32) is used as an interface platform to enable real-time data collection for performing EIS. Figure 3.8(b) illustrates the experimental setup, where an IDE is immersed in 15 ml sugar solution (1% W/V). The amount of yeast is varied through out the experiment. The IDE is connected to the prototype PCB with a JST connector. The phase and magnitude data from AD5933 is transferred to a PC via USB-to-Serial connection for further processing and recording. As shown in Figure 3.8(c), for solution with no yeast, the measured R_{sol} is about 2.63 k. For yeast concentration of 0.2% W/V, R_{sol} reduces by 30.14% to about 1.8 k. Further increase in yeast concentration result in reduction in R_{sol} value. These findings demonstrate the potential of the proposed impedance spectroscopy-based system for ZnO based-nanorods IDE for detecting and analyzing micro-organisms.

3.5 Conclusion

In this paper, a portable integrated system for micro-organism detection has been presented, which is based on electrochemical impedance spectroscopy. The proposed system includes Zinc Oxide (ZnO) nanorods based interdigitized electrode (IDE) sensor and an EIS circuit. This work also presented the considerations and methodology for the fabrication of ZnO nanorods with high-yield. To validate the efficacy of the proposed methods, experimental results through scanning electron microscope are presented. Finally, measurement results for detection of a micro-organism (yeast) is also presented to demonstrate the utility and effectiveness of the proposed methods and system.

Chapter 4

GoldAid: Industry Safety System for Enabling Rapid Medical Aid in the Golden Hour

4.1 Introduction

Operation and maintenance activities of industries such as thermal power plants, nuclear plants, natural gas exploration plants, and mines often require a large number of employees to work under challenging conditions, which pose significant risks to their health and lives. For example, maintenance of tall chimneys requires cleaning and repairing aviation lights and gas sensors, which expose plant workers to considerable risks of falling from greater heights (> 20 m). Industrial environments also house zones with high temperature and hazardous gases like Carbon monoxide (CO) and Methane (CH₄), which present a significant safety threat to workers if exposed for prolonged time [36], [37].

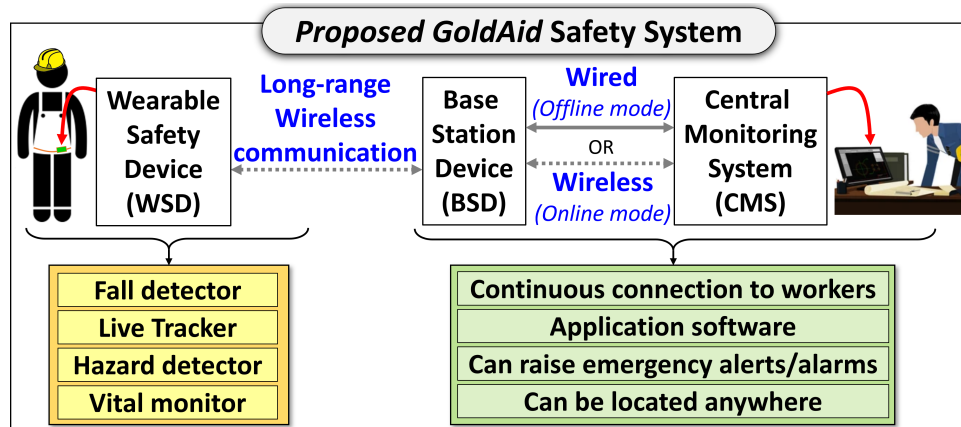


Figure 4.1: Proposed *GoldAid* Safety System

Industries equip the workers with various safety gear such as harnesses, helmets, boots, respiratory protection, and other work environment-specific gear. However, occupational accidents remain a persistent issue in large-scale industries. According to the International Labor Organization (ILO), ap-

proximately 2.3 million workers succumb to work-related accidents every year [38]. Among these, fall from heights is the greatest cause leading to 48% serious injuries and 30% fatalities [39]. The main reason for fatal outcomes is the delay in reporting the accidents, which causes delay in receiving the essential medical aid in the most critical first sixty minutes (golden hour) after the accident.

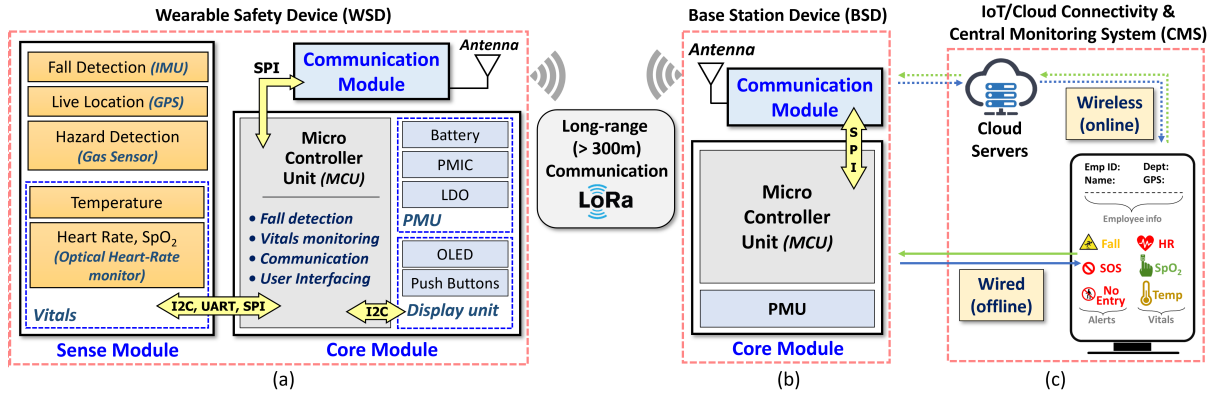


Figure 4.2: Architecture of the proposed: (a) Wearable Safety Device (WSD) (b) Base Station Device (BSD) (c) Central Monitoring System (CMS)

Some commercial products, which emerged in the recent past can be utilized to address this concern [40, 41, 42, 43, 44, 45]. However, most of these devices require LTE/Satellite communication with continuous in-field internet connectivity, which is expensive and might be unavailable in industries at remote places and mines [42, 43, 45, 44]. Some of these devices do not have provision to monitor body vitals of workers [41, 42, 43, 45, 44]. Moreover, the fall detection mechanism in these devices do not cover all possible scenarios of industrial fall such as fall of workers from great heights or during daily activities and fall of equipment (elevator, crane). Therefore, there is a need for a customisable, scalable, reliable, and low-cost safety solution, which can be easily adopted by different types of large and small scale industries. In this research, we leverage the advancements in sensor integration, wireless communication, wearable and Internet-of-Things (IoT) technologies and propose a safety system *GoldAid*, which addresses all the industrial needs to enable the fastest medical aid in the golden hour.

Figure 4.1 depicts the proposed *GoldAid* system, where a battery-operated wearable safety device (WSD) captures and processes worker’s data (fall incidence, location and body vitals), and transfers it in real-time by using a long-range (>300 m) communication protocol to a base station device (BSD). The BSD connects with a central monitoring station (CMS) through an IoT cloud or direct-wired means, where an application software is used to monitor and manage worker data. It can also send/receive emergency alerts to/from WSD. The key contributions of this work are as follows:

1. Integration of numerous sensors in an IoT framework is presented to achieve an accurate, fast, energy-efficient safety system suitable for diverse industries.

2. For all potential fall scenarios of workers, Convolutional Neural Network (CNN) based fall detection algorithm is proposed. Moreover, for detecting fall of equipment and machinery, a low power acceleration-threshold based technique is also presented. The proposed methods can precisely detect all industrial falls from heights >10 meters and from surfaces < 2 meters.
3. A versatile and scalable model for deploying multiple WSD and BSD to ensure continuous coverage in large-scale industrial setup has been presented. With the proposed methods, a low-power realization of long-range (>300 m) communication using 433 MHz LoRa protocol is presented, which achieves high wireless reliability ($BER < 3 \times 10^{-4}$) and low latency (< 1 s).
4. The hardware design considerations for implementation of the proposed fall detection methods, vital monitoring, and location tracking on a portable embedded platform is presented and a battery operated, ergonomic, low-cost system prototype is developed.
5. To prove the utility of the proposed *GoldAid* system in actual operating scenarios, end-to-end experimental results from a thermal power plant are also presented.

The paper is organized as follows: Section 4.2 presents the system architecture of the proposed *GoldAid* system. Section 4.3 provides a functional implementation of proposed fall detection models (threshold and CNN-based), while the full system implementation details with design considerations are described in Section 4.4. Section 4.5 presents the measurement results, and Section 4.6 concludes the paper.

4.2 System Overview and Architecture Details

Figure 4.2 depicts the detailed architecture of the proposed *GoldAid* System, which comprises of - 1) WSD, 2) BSD and 3) IoT connectivity with application interface for CMS. Succeeding sub-sections present details of these building blocks.

4.2.1 Wearable Safety Device (WSD)

Figure 4.2(a) shows WSD comprising sense, core and communication modules, which are described below.

4.2.1.1 Sense module

As illustrated in Figure 4.2(a), sense module incorporates various sensors enabling a wide range of features. This includes accelerometer and gyroscope for fall detection, Global Positioning System (GPS) for location tracking, gas sensors for hazard sensing, temperature sensor and photoplethysmography (PPG) sensor for vital monitoring [46, 47, 48, 49]. As shown in Figure 4.2(a), signals from sense module are serially transferred to the core module, which is discussed next.

4.2.1.2 Core module

As shown in Figure 4.2(a), the core module comprises a microcontroller unit (MCU), a power management unit (PMU), and a display unit. MCU controls the overall functioning of the WSD. It gathers and processes signals from sense module to detect falls, location and body vitals. MCU executes the proposed CNN based fall detection algorithm and identifies anomalies in vital and location information. WSD operates on a lithium polymer (LiPo) battery, which, when coupled with a power management IC (PMIC) and a low-dropout (LDO) voltage regulator, forms the PMU [50]. As shown in Figure 4.2(a), the core module also features a display unit which comprises OLED screen and dual push buttons to provide a simple user interface. The processed sensor data from the core module is sent to the communication module for further transmission.

4.2.1.3 Communication module

As shown in Figure 4.2(a), the proposed system uses LoRa communication protocol, leveraging its advantages such as low latency, long range, and low-power consumption for prolonged battery life of the device. Direct transmission of worker data to CMS for surveillance is difficult due to the vast size of industries. Therefore, the processed data at WSD is first sent to base station device (BSD), which acts like a bridge device between WSD and CMS. The architecture of the BSD is explained in the next sub-section.

4.2.2 Base Station Device (BSD)

As depicted in Figure 4.2(b), architecture of BSD comprises of a core and a communication module. The purpose of communication module is to receive data signals from WSD and pass it on to the core module. The data in core module is organised, processed and subsequently handed over to the communication module, ready for transmission to the CMS, employing either of the following methods: 1) wired transmission, where BSD is connected to the CMS using cables which is suitable for offline operation in remote areas 2) wireless transmission, where BSD is connected to the Internet, allowing it to communicate with CMS via cloud servers. In the latter configuration, BSD functions as a LoRaWAN gateway [51]. To ensure seamless communication within an industry employing numerous workers, the BSD is also responsible for handling communication with multiple WSDs without data loss.

4.2.3 IoT connectivity and application interface for CMS

As depicted in Figure 4.2(c), CMS in the proposed system contains an application interface to efficiently retrieve, process, and monitor worker data (fall status, live location, health metrics & hazard information) from the signals received at BSD. Additionally, CMS also issues alerts in response to the emergencies like falls or SOS signals triggered by workers.

As discussed in the Section 4.2-A, WSD incorporates the proposed fall detection algorithms for covering all types of industrial fall scenarios. The methodology of the developed algorithms is discussed in the next section.

4.3 Proposed Fall detection Methods

To detect a broad range of fall incidents across various industries, this work presents two algorithms based on - 1) Machine learning and 2) acceleration-threshold techniques. The proposed methods efficiently detect falls from heights (FFH), such as those from high platforms or chimneys, and same floor falls (SFF), which includes falls during activities like walking or standing. Moreover, the proposed methods automatically reports fall events in real-time and estimate fall height/type, with very low latency. Further, to reduce false fall detection among workers, the proposed methods distinguish between activities of daily living (ADL) like brisk walking, hammering, heavy lifting, and actual falls. To develop the proposed algorithms, investigation of different fall and ADL is done with the help of a test hardware. Details of the test hardware, setup for collecting the data for ML model training and the proposed fall detection algorithms are discussed next.

4.3.1 Test Hardware and Experiments for Data Collection

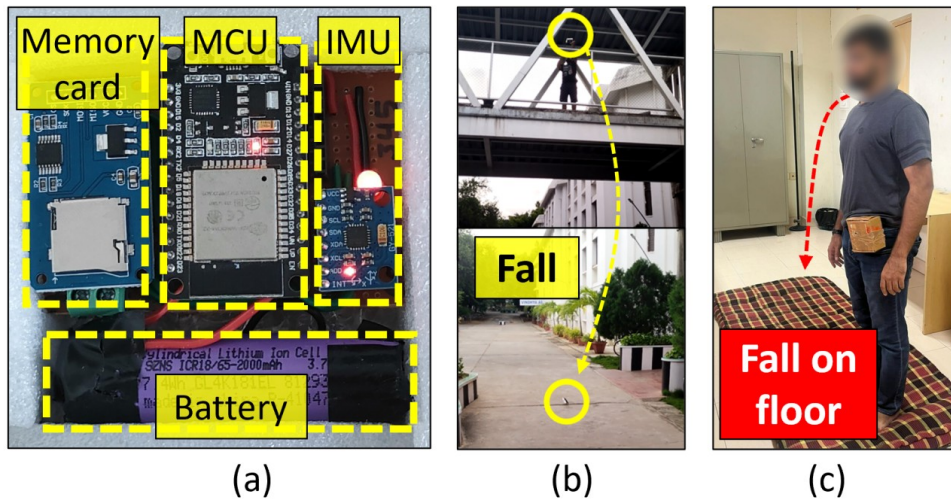


Figure 4.3: (a) Circuit design of the setup (b) Fall testing from heights (>5 m) (c) Same floor fall testing

Figure 4.3(a) shows the developed battery operated hardware for capturing acceleration values a_x , a_y , and a_z in x, y and z directions, respectively. It includes an inertial measurement unit (IMU), which comprises of 3-axes accelerometer and 3-axes gyroscope to measure linear and angular acceleration values, respectively. A memory card and an MCU is also integrated in the hardware for logging acceleration data and its processing, respectively. The a_x , a_y , and a_z values recorded from the test hardware

are used in estimating the sum vector magnitude (SVM) a_m given by Eq. 4.1 [52], which is further used for the development of the proposed fall detection algorithms.

$$a_m = \sqrt{a_x^2 + a_y^2 + a_z^2} \quad (4.1)$$

Figure 4.3(b) shows the experimental setup, where the test hardware is dropped from different heights of a building to collect data for FFH scenario. Figure 4.3(c) depicts the experimental setup for SFF and ADL, where the test hardware was mounted on the waist of a subject, who performs various fall and daily activities in a controlled environment. Table 4.1 summarizes the experimental data collected for the development of the proposed fall-detection algorithms. This includes 1) 150 tests for FFH, 2) 135 tests for SFF and 3) 120 tests for ADLs. Acceleration values for these experiments are sampled at a rate of 250 Hz, which is greater than twice the human’s activity frequency band which is around 100 Hz to achieve oversampling [53, 52]. Figure 4.4 depicts the acceleration magnitude vs time graphs for a few scenarios of falls from different heights and ADLs recorded during the testing. In Figure 4.4(a), we observe a distinct spike ($> 10g$) in acceleration values indicating of an impact after a fall. This is in contrast to the lower acceleration levels ($< 3g$) seen during ADL as depicted in Figure 4.4(b). These findings help in setting a reliable threshold acceleration value for both of the proposed fall detection methods. The development details of the algorithms are discussed in the following subsections given below.

Table 4.1: Summary of data collected

Category	Activity	No. of tests
Fall from heights (FFH)	<1 m	30
	1-2 m	30
	2-5 m	30
	5-10 m	30
	10-20 m	30
Same floor falls (SFF)	Backward	45
	Forward	45
	Side-ward	45
Activity of daily living (ADL)	Running	30
	Walking	30
	Sitting/Standing	30
	General Activities	30

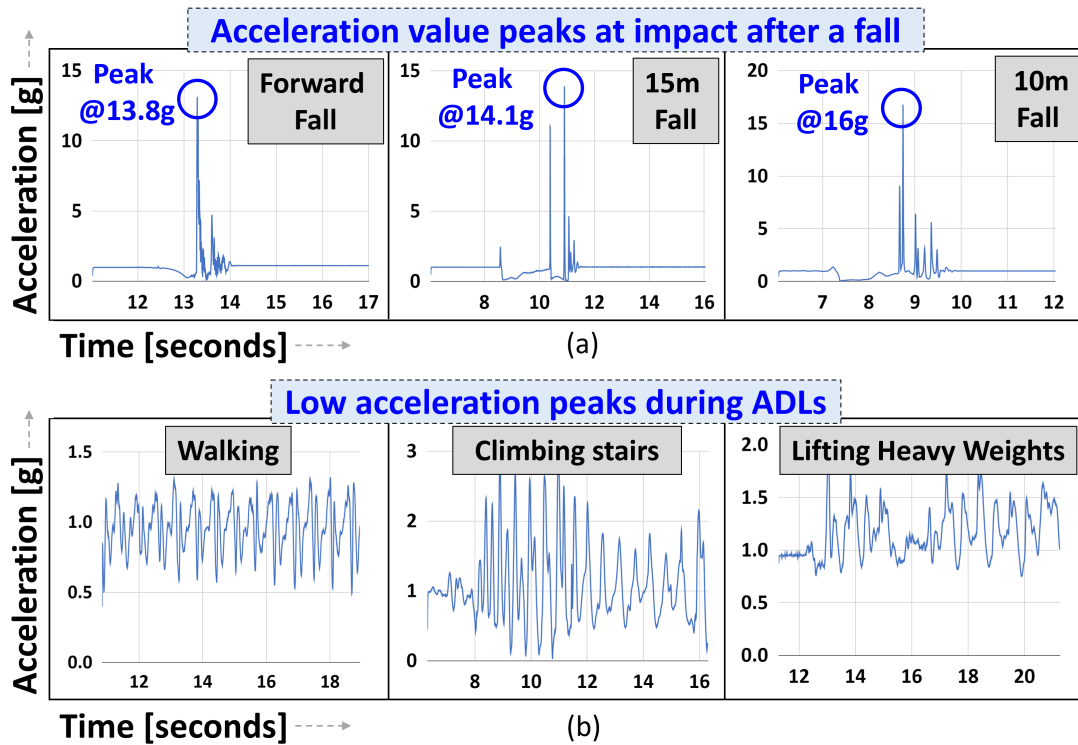


Figure 4.4: Plot of acceleration vs time for (a) Falls (b) ADL

4.3.2 Algorithm-1: Machine Learning (ML) approach

Table 4.2: ML model comparison on SisFall data set [54]

	SVM	KNN	XGB	MLP	CNN
Accuracy	0.9752	0.9836	0.9710	0.9979	0.9987
Sensitivity	0.9176	0.9088	0.9235	0.9853	0.9824
Specificity	0.9765	0.9852	0.9721	0.9982	0.9990

In the event of a human fall, the body undergoes both linear and rotational motions[55]. To detect this combined motion pattern and accurately differentiate between FFH, SFF, and ADL, we propose an ML based technique. In this technique, three-axes accelerometer and gyroscope values are fed to the proposed ML model, which is employed on an embedded platform at WSD. To find the most appropriate ML model for the application, different models like Support Vector Machines (SVM), K-Nearest Neighbour (KNN), Convolutional Neural Networks (CNN), and Multilayer Perceptron (MLP) were trained and evaluated [56, 57, 58] on an existing Sisfall database [54], which comprises of acceleration data for various kinds of falls and daily activities. Table 4.2 compares these models based on accuracy,

sensitivity, and specificity values, which shows that CNNs and MLPs outperform other models, notably by eliminating the need for feature extraction in both training and testing. They excel in recognizing complex patterns within raw data, improving prediction accuracy. Their efficient information extraction streamlines models, reducing resource usage and enhancing training effectiveness [59]. Among these two choices, CNN is finally selected as it minimizes the computation cost to an embedded MCU [60].

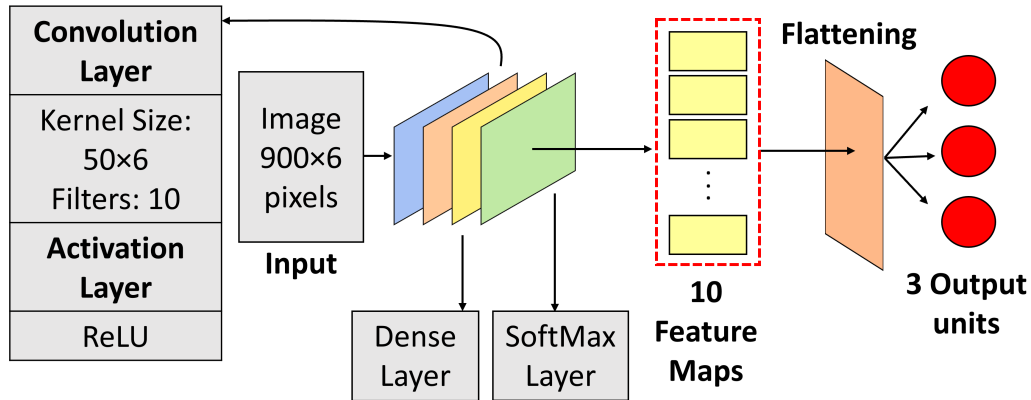


Figure 4.5: Architecture of proposed ML model architecture

Figure 4.5 shows the detailed network of the proposed CNN model, which consists of one convolutional layer of ten neurons, with a rectified linear unit (ReLU) activation layer [61], followed by one dense layer of two neurons with a soft-max activation layer at the end. The CNN layer has a kernel size of (50,6) and a stride of 5, giving approximately 4500 parameters. We capture linear and angular acceleration of three dimensions, yielding 6 values per sample. Peaks in acceleration trigger the input of values from a 3.6-second window (900 samples at 250 Hz) to the model as an image. After convolution, 10 feature maps emerge, flattened using a linear layer for classification among SFF, FFH and ADL. The proposed CNN model is trained, tested and verified with a split ratio of 60:20:20. For training, Synthetic Minority oversampling technique (SMOTE) is used to fix the class imbalance along with random under-sampling to optimize it for better accuracy [62]. To implement the proposed model on a portable platform, i.e. embedded MCU, design considerations are discussed in Section 4.4-A.

4.3.3 Algorithm-2: Acceleration-threshold approach

This method is ideal for power-efficient devices, offering high accuracy and sensitivity for FFH, which typically involves a straight-line fall along a single axis due to gravity's pull. The algorithm utilises only three-axis acceleration data as input, and can operate on a low-power MCU. Due to the use of minimal resources, it is most suited for identifying falls in heavy objects and machinery like elevators and cranes.

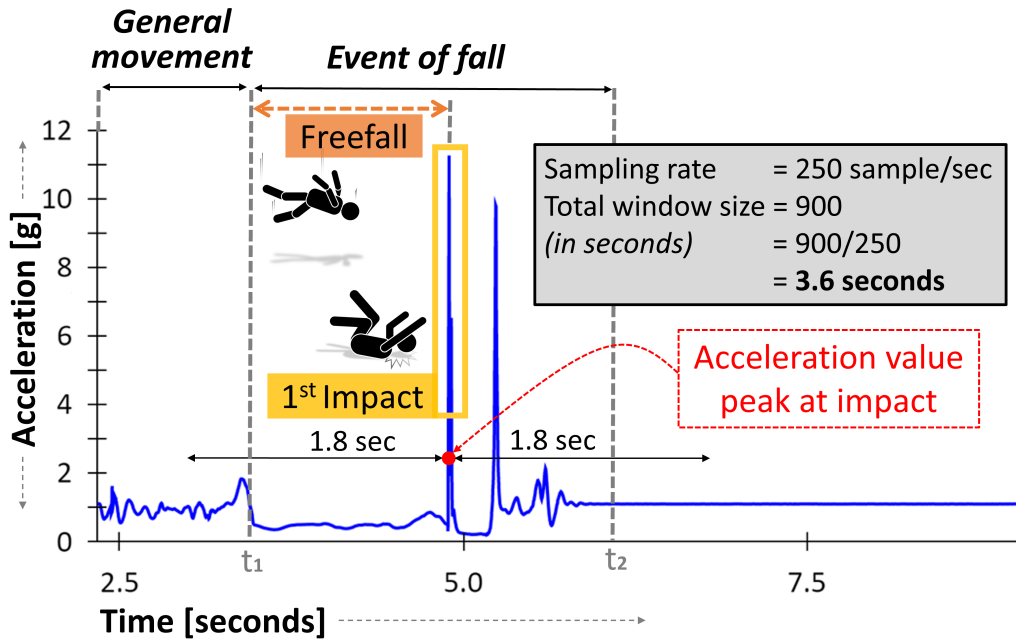


Figure 4.6: Representation of fall on an acceleration vs time plot

Figure 4.6 depicts the characteristic acceleration profile of a fall from a height (FFH). During FFH, a body experiences weightlessness, confirmed by the sudden dip in acceleration readings from the plot. The fall is confirmed with a high peak in acceleration indicating an impact on a hard surface. Therefore, the main events to detect a linear fall are identified as [63]:

- **Free fall:** It is the condition when the acceleration magnitude of a body ideally reaches a value of $0g$, and the freefall duration depends on height of the fall.
- **1st Impact:** The subject experiences this when it first hits a hard surface after a free fall. In this case, a sharp peak in acceleration magnitude is noticed as depicted in Figure 4.4(a).

Algorithm 1 shows the proposed acceleration-threshold based fall detection approach, which takes acceleration values of the three axes as the input.

Algorithm 1 Fall Detection Algorithm

Real-time acceleration values of the body Fall detection confidence level

$fall_flag \leftarrow False; fall_count \leftarrow 0; total_count \leftarrow 0$

$FF_acc_threshold \leftarrow 0.8g$ *Desired threshold value

while real-time data collection **do** Calculate acceleration SVM using equation (1)

if SVM < FF_acc_threshold **then**

if fall_flag **is** False **then** $fall_flag \leftarrow True$ "Freefall start at t_1 " $fall_count \leftarrow 0; total_count \leftarrow 0$; counters

else $fall_count++$ $confidence \leftarrow fall_count / total_count$ $total_count++$

if (time - $t_1 > FF_time_threshold$) **and** (confidence > 0.9) **then** $fall_certain \leftarrow True$

if (SVM > impact_acc) **and** (fall_certain **is** True) **then** "Fall Detected at t_2 "

SVM of acceleration values is calculated using Eq.(4.1) at a rate of 250 samples per second. As depicted in Figure 4.6, the fall starts from a free-fall condition at time t_1 , where the acceleration experienced by the subject should ideally be zero. However, due to air resistance and irregularities in the motion of the falling body, the acceleration value is marginally greater than zero. Therefore, the algorithm continuously checks for SVM values below a free-fall acceleration threshold defined by the $FF_acc_threshold$ variable. When this condition is met, the $fall_flag$ is set to TRUE and $fall_count$ is incremented by one. The algorithm defines $confidence$ as the ratio of number of samples below the $FF_acc_threshold$ and the total number of samples. If this condition persists for a time span greater than $FF_time_threshold$ and with a high confidence level, it indicates the possibility of a fall. Subsequently, the algorithm searches for a peak, defined by acceleration value greater than the threshold $impact_acc$. The occurrence of this peak confirms the 1st impact of the test subject on a hard surface validating the occurrence of a fall, after which a notification containing the details and location of the fall is sent to the CMS by the MCU. Also the height of the fall is determined on the basis of freefall duration using Newton's 2nd equation of motion:

$$s = u\Delta t + 0.5a(\Delta t)^2 \quad (4.2)$$

where, s is the height of the fall, u and a are the initial velocity and the acceleration of the falling body respectively. Δt is the fall duration given by $t_2 - t_1$.

The threshold values are determined based on an empirical investigation of various fall scenarios. The value of $FF_time_threshold$ is set to 500 milliseconds to detect falls of heights >1.225 meters which is calculated using (4.2). The peak acceleration threshold value defined by $impact_acc$ is set to 5g since the maximum acceleration value associated with ADL is considerably lower. Furthermore, a $FF_acc_threshold$ of 0.8g and value of $confidence$ of 0.9 is chosen as they produce the best sensitivity and specificity when utilized in the algorithm.

4.4 Hardware Implementation

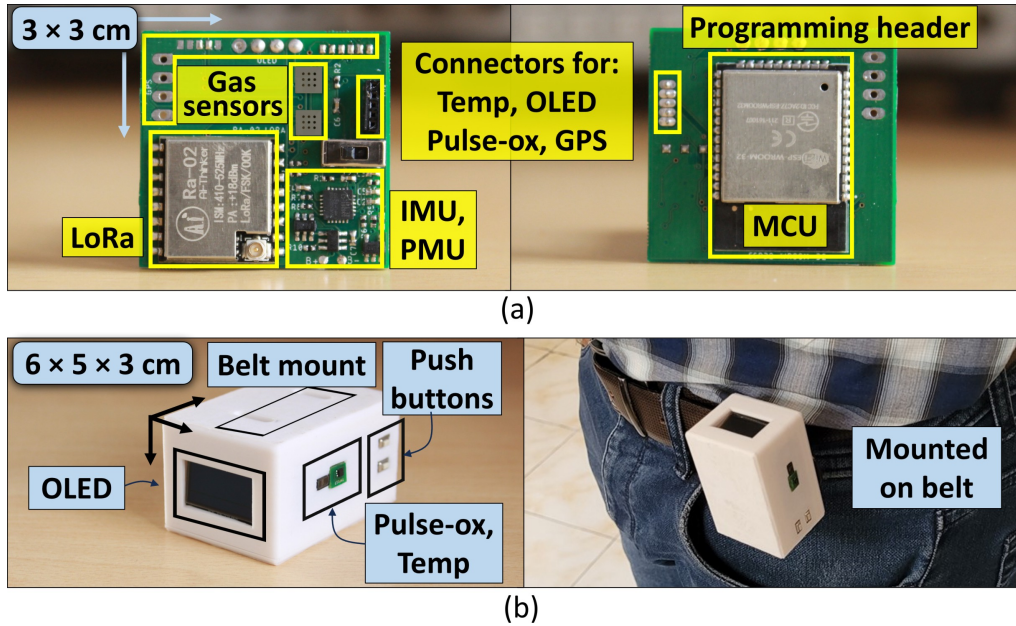


Figure 4.7: (a) Top and bottom view of integrated PCB (b) 3D Printed Enclosure

Figure 4.7(a) shows the custom-designed printed circuit board (PCB) measuring 3×3 cm to integrate all features. It fits in a 3D printed enclosure for a waist-mounted WSD with dimensions of $6 \times 5 \times 3$ cm, as in Figure 4.7(b). Detailed hardware implementation and design considerations for each module of the WSD are discussed in further sub-sections.

4.4.1 Sense Module

The components used for implementing different features of the sense module are discussed below:-

4.4.1.1 Fall detection

Figure 4.7(a) shows the presence of an IMU, which is MPU-6050 from InvenSense [64], which can measure linear and angular acceleration upto $\pm 16g$ and $\pm 2000^\circ/\text{sec}$ respectively. The acceleration data from the sensor is transferred to the MCU via Inter-Integrated Circuit (I^2C) communication protocol, which is then processed for detecting falls. The proposed CNN model outlined in Section 4.3-A is developed and tested in Python. To detect falls in real-time, the ML model has to execute on the MCU-ESP32 present on the WSD, for which the following modifications are made:

- The number of neurons, stride, and window length is decreased to 10, 30, and $\pm 450/250$ respectively to reduce memory usage[65]

- TensorFlow model is converted to TensorFlow lite model
- Conversion of the model from Python to a C byte array using tinymigen [66] to store it in flash memory of MCU

These changes made it possible to load the ML algorithm on the MCU along with the firmware for other modules. Detailed discussions on the measurement results of the proposed model can be found in Section 4.5-A.

4.4.1.2 Live tracking and Hazardous zone detection

The WSD incorporates an integrated SIM28ML module 10.1×9.7×2.5 mm using UART on the ESP32’s second serial port for GPS location acquisition. The module consumes 16 mA during tracking and comes with a built-in antenna. To ensure worker safety in environments with hazardous gases, MEMS-based Carbon Monoxide (CO) and Hydrogen Sulfide (H₂S) gas sensors are integrated. Evacuation alerts are triggered if CO levels are > 400 ppm or H₂S levels exceed 15 ppm [67]. These alerts, along with worker location data, are transmitted to the CMS. Additionally, other gas sensors can be integrated according to the specific industrial requirement.

4.4.1.3 Vitals



Figure 4.8: WSD’s OLED depicting different prompts

Protocentral’s MAX30102 module with integrated MAX32664 has been used to measure heart rate (HR) and blood-oxygen saturation (SpO₂) [68] by performing photo-plethysmography (PPG) [69]. The MAX32664 sensor hub IC processes the raw analog values from the MAX30102 AFE to measure HR and SpO₂[70, 71]. Temperature readings are obtained using Texas Instrument’s contact-based TMP117 sensor[72], offering a resolution of 0.0078°C and an accuracy within ±0.1°C. To conserve power, the sensor has been configured in one-shot conversion mode, after which it goes into low-power shutdown mode. For accurate readings, the fingertip is chosen as the optimal measurement location as it prevents the user from engaging in other activities minimizing motion-related uncertainties [73].

4.4.2 Core Module

The MCU used is ESP32-WROOM-32D, well-suited for our requirements due to attributes like processing, memory, size, cost, ML compatibility, and power management [74]. It executes the proposed ML model for fall detection and manages all other system modules simultaneously. Figure 4.7(b) shows the presence of an OLED display and two push buttons on the WSD to provide an user-interface to the worker. Figure 4.8 depicts the prompts displayed on OLED for different scenarios. Also, in case of emergencies, a worker can long-press both push-buttons to initiate an SOS alert to the CMS.

4.4.3 Communication Module

Ai-Thinker's Ra-02 [75] LoRa transceiver module is used to enable long-range communication to BSD. It connects to the MCU via Serial Peripheral Interface (SPI) protocol.

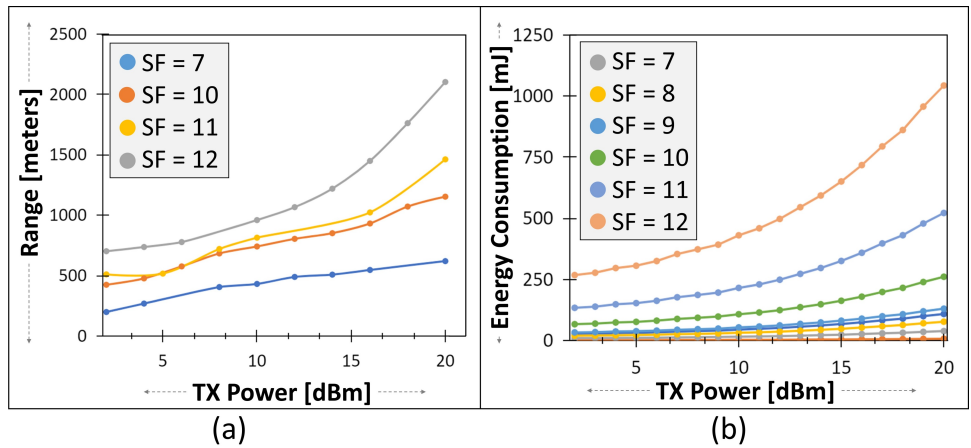


Figure 4.9: (a) Range vs TP (b) Energy vs TP for different spreading factor

As shown in Figure 4.9, maximum transmission power (TP) and spreading factor (SF) settings result in an impressive line of sight (LOS) range at the cost of high energy consumption (>1000 mJ). This significantly impacts the battery life of the device. Therefore, for optimal performance, the TP and SF values are set to 14 dBm and 10 respectively. Additionally bandwidth (BW) of 62.5 kHz and coding rate (CR) of 8 is set, which results in an LOS range of >300 meters with a energy consumption of 115 mJ.

4.5 Measurement Results

4.5.1 Individual Module testing

4.5.1.1 Measurement results for fall detection

Table 4.3: Threshold-based fall detection algorithm testing results

Fall height [m]	<1	1-2	2-5	5-10	10-20	ADL
No. of falls	12	15	13	18	16	30
Detected	10	13	12	17	15	28
Sensitivity [%]	83.34	86.67	92.30	94.45	93.75	93.34

Table 4.4: Comparison of developed ML model with others [76]

Model	Sensitivity [%]	Specificity [%]
Logistics Regression	95	92
Naïve Bayes	99	91
Nearest Neighbour	90	96
Decision Tree	94	96
Support Vector Machine	96	96
This work	98.87	97.83

Table 4.5: Comparison between two proposed fall detection methods

Method	Latency	Memory requirement	
		RAM	ROM
Threshold based	34 μ s	607	15402
ML based	8 ms	50288	138513

The performance of the proposed fall detection algorithms can be analyzed using the sensitivity and specificity values. These values are defined as:

$$Sensitivity = \frac{TP}{TP + FN}, Specificity = \frac{TN}{TN + FP} \quad (4.3)$$

True positive (*TP*): Fall occurred, detected

True negative (*TN*): Fall not occurred, not detected

False positive (*FP*): Fall not occurred but detected

False negative (*FN*): Fall occurred, not detected

As discussed in Section 4.3, threshold values are empirically set to fine-tune the algorithm's performance. Table 4.3 shows the results of the threshold-based algorithm, detecting 67 falls out of 74 instances and 28 ADLs out of 30 instances. Sensitivity, calculated using (4.3), is 90.54%.

The ML-based fall detection algorithm achieves an accuracy of 99.52%, with specificity of 98.87% and sensitivity of 97.83%. Table 4.4 compares our proposed ML-based algorithm with prior art on the basis of sensitivity and specificity values. Table 4.5 presents a comparison of the memory requirements for the proposed fall detection algorithms. It can be inferred that there is a trade-off between accuracy and memory requirement. While the ML-based approach offers higher accuracy, it necessitates a substantial memory allocation for its execution.

4.5.1.2 Communication range testing and power consumption

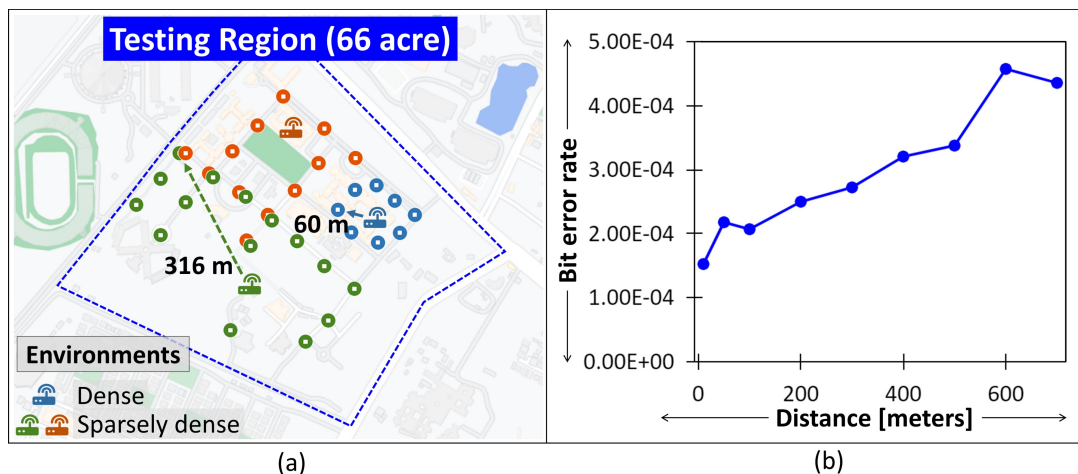


Figure 4.10: (a) Map with marked points with the successful transmission (b) Bit error rate (BER) vs Distance plot for Line of Sight (LOS) experiment

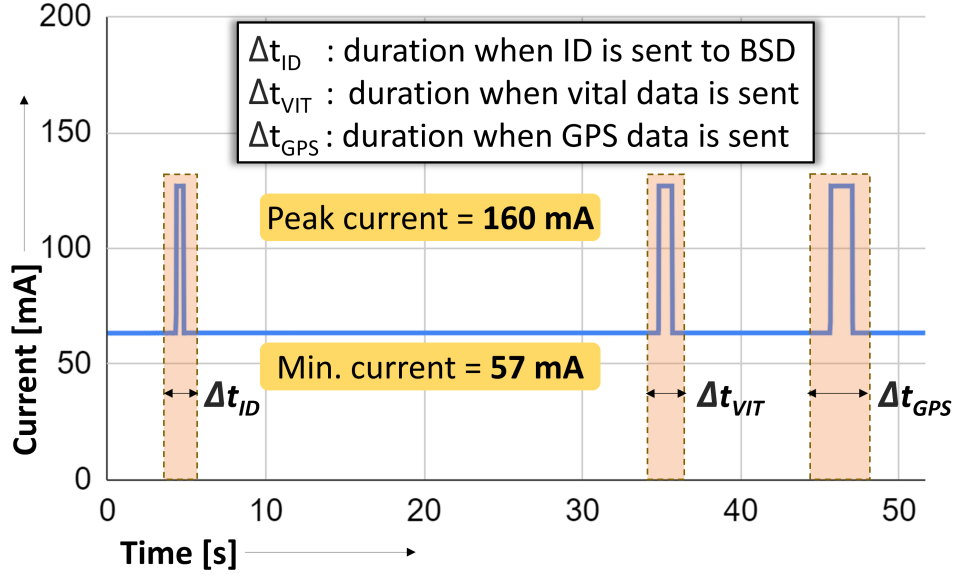


Figure 4.11: Current consumed by i^{th} WSD in one iteration vs Time plot

The system's feasibility and scalability were assessed through a LoRa communication test across a 66-acre campus. This test utilized 3 BSDs and 8 WSDs to ensure comprehensive coverage. It involved real-time tracking of individuals equipped with WSDs as they moved within specified zones, transmitting vital and location data. Using GPS coordinates, Figure 4.10(a) demonstrates the system's maximum range: 60 meters in densely populated areas and 316 meters in less crowded ones. Figure 4.10(b) showcases the achieved bit error rate (BER) for 16 KB data transmission.

$$Hours = \frac{(Battery\ capacity) \cdot (T_{rx})}{(T_{peak}) \cdot (Peak\ current) + (T_{rx} - T_{peak}) \cdot (Min.\ current)} \quad (4.4)$$

where, $T_{peak} = (\Delta t_{ID}) + (\Delta t_{VIT}) + (\Delta t_{GPS})$

In addition to the LoRa configurations discussed in Section 4.4-B, the WSDs' *waiting_window* and *beacon_interval* parameters were set to 30s and 10s respectively. This configuration facilitates the integration of new WSDs into the network and ensures optimal data reception. With the values depicted in Figure 4.11, the battery life of *GoldAid* WSD is estimated at 18 hours, as determined by (4.4). Here, T_{rx} is fixed at 15 s, while T_{peak} is experimentally measured at 1.5 s.

4.5.2 Full system testing in a live environment

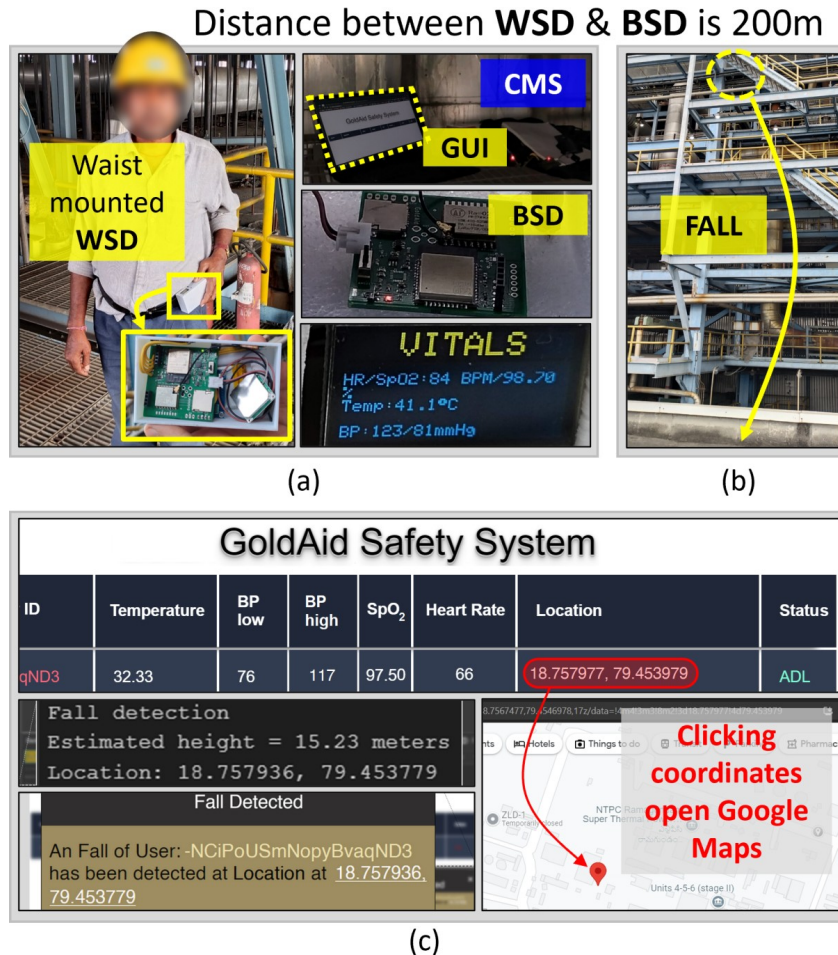


Figure 4.12: (a) WSD mounted on the worker’s waist and BSD setup at a distance around 200 meters (b) Simulating a fall from an approximate height of 15 meters for testing fall detection algorithm (c) Developed GUI for the central monitoring purposes

Figure 4.12 depicts the testing of the *GoldAid* system in an thermal power plant. A worker, as seen in Figure 4.12(a), wore the WSD on his waist, which is wirelessly connected to the BSD located 200 m away, which is connected to the internet. The notifications prompted the worker to use the fingertip pulse-ox sensor on the WSD to measure vital signs. In Figure4.12(b), a fall simulation is executed by dropping a dummy weight from a 15-meter height. Fall alerts, along with fall height, location, and vital signs, are transmitted from the WSD to the BSD and subsequently sent to a ThingSpeak cloud server. To facilitate user-friendly data retrieval, an application interface is developed for CMS as shown in Figure 4.12(c). Table 4.6 compares *GoldAid* to other existing commercial wearable safety devices.

Table 4.6: Comparison of *GoldAid* with commercial safety devices

Device	Vitals	Fall detection	SOS	Communication	User Interface	Cost
TCS IoT Safety Watch [40]	HR SpO ₂	Yes, immobility detection	Yes	LoRaWAN	OLED	-
Triax Spot-r Mesh [41]	-	Yes	Yes	-	LCD	-
Tended Protect [42]	-	Yes, no motion detection	Panic Alarm	Cellular, WiFi	OLED	\$78
Black-line G7 lone worker [43]	-	Yes	Yes	4G/3G Satellite	Push Buttons	\$792
Reactec RASOR [44]	-	Yes	Panic Alarm	GSM	-	-
Lifecall Advanced Mobile [45]	-	Yes	SOS	4G	Push Button	\$494/year
<i>GoldAid</i> (This work)	HR, SpO₂	Yes (ML - SFF, FFH Threshold - FFH)	Yes	LoRaWAN	OLED, Push Buttons	< \$60

4.6 Conclusion

This research proposes a safety system for industrial environments, enhancing worker safety. Through sensor integration, the system monitors health, real-time status, and precise locations. The work introduces two methods: a machine-learning model with 99.52% accuracy for human fall detection and an efficient threshold-based approach for machinery-related falls. Furthermore, the paper addresses hardware design and communication configuration, achieving an impressive combination of extended range (>300 m) and an optimal 18-hour battery life. The system achieves a bit-error rate of less than $<3 \times 10^{-4}$. It also proposes a strategy for scalable communication systems, extending coverage, minimizing power consumption, and ensuring noise-free data transmission. Workers can transmit and receive SOS signals using the proposed device. To validate the system's effectiveness, extensive testing was conducted in a thermal power plant. This real-world application highlights the system's practical utility, acceptance, and potential to significantly elevate workplace safety.

Chapter 5

Conclusions and Future Work

5.1 Research Contributions

This thesis has showcased numerous advancements in healthcare sensing, particularly in domains like elderly care, critical care units, and prolonged home monitoring, where continuous monitoring of vital signs is essential. Within this scope, the utilization of FMCW radars stands out as a common non-invasive method. The thesis has introduced Mixer-first based Receiver front-ends as a means to enhance system linearity. Additionally, a circuit technique has been proposed and implemented in TSMC 65 nm technology node to address phase errors in non-overlapping LO pulses, effectively validating the wide-band operation of the N-Path mixers across the 8-20 GHz frequency range. The finalized design has been submitted for fabrication, marking a significant step forward in advancing the capabilities of healthcare sensing technologies. The key points of this contribution are:

- Implemented 8-20 GHz 4-Path Receiver front-end in TSMC65nm PDK
- The Designed circuit covers an area of $600\mu\text{m} \times 300\mu\text{m}$ and has been fabricated
- Programmable gain of 10-29 dB using 8-bit programmable resistor bank
- Proposed design achieves an IIP3 of >-10 dB, S11 of <-12 dB
- Total power consumption stands at 66 mW from a 1.2 V supply

Furthermore, expanding the scope of healthcare sensing, this thesis introduced a micro-organism detection system leveraging electrochemical impedance spectroscopy (EIS). A portable and cost-effective impedance analyzer was designed specifically to measure the impedance of a bio-sensor based on gold-plated ZnO Nanorods. The key points of this contribution are:

- Presented design considerations and methodology for the fabrication of ZnO nanorods with high-yield
- Experimental results through scanning electron microscope are presented

Additionally, this research introduced an industry-tailored system named "*GoldAid*." By integrating sensors within an IoT framework, GoldAid successfully accomplished continuous monitoring of vital

signs, fall detection, and real-time location tracking of workers within expansive industrial environments. The key points of this contribution are:

- The Proposed system is capable of monitoring workers' health and live location and can detect falls for humans and machinery
- A machine-learning model with 98.44% accuracy in human fall detection is proposed
- A method for detecting machinery-related falls that is efficient in terms of both resource usage and time is presented
- The system achieves a communication range of 300 meters, with a bit-error rate of $<3 \times 10^{-4}$

5.2 Future Works

The Receiver front-end developed in this thesis had a 20 dB roll-off at the RF port, which can be improved to a higher-order roll-off to increase the receiver's in-band linearity and blocker tolerance. This can be done by increasing the attenuation order at the IF port with capacitive positive feedback or shunt feedback technique. Currently, the generation of non-overlapping quadrature LO pulses requires differential sinusoidal pulses through external means. This can be improved by implementing an on-chip balun, which will ease the input requirements.

The *GoldAid* industrial safety system showcased the development of a waist-mounted wearable device. By compacting the design of the prototype PCB, a wrist-based wearable can be developed. This can be done using alternate modules for LoRa communication and GPS.

Related Publications

Accepted Publications

1. **A. Sahni** and A. Srivastava, "Design of a Wideband 8-20 GHz Receiver Front-End with Reduced Local Oscillator Phase-Error in 4-Path Mixer" 2023 19th IEEE Asia Pacific Conference on Circuits and Systems (APCCAS), Hyderabad, India, 2023
2. **A. Sahni***, K.V. Varma*, Deeksha, B. Ghosh, A. Sarje, and A. Srivastava, "Design of Integrated System for Detection of Micro-organisms with Fabrication and Testing of ZnO Nanorods based Biosensor" 2023 IEEE Biomedical Circuits and Systems Conference (BioCAS), Toronto, Canada, 2023 (**Equal contribution*)
3. S. S. Chatterjee, **A. Sahni**, H. Kambham, and A. Srivastava, "Design and Analysis of Low Power 20 GHz Colpitts VCO with FoM of 196.26 dBc/Hz," 2023 IEEE 66th International Midwest Symposium on Circuits and Systems (MWSCAS), Phoenix, Arizona, USA, 2023
4. S. Mantha, A. S. Edakkadan, **A. Sahni**, and A. Srivastava, "An mmWave Frequency Range Multi-Modulus Programmable Divider for FMCW Radar Applications," 2023 36th International Conference on VLSI Design and 2023 22nd International Conference on Embedded Systems (VLSID), Hyderabad, India, 2023, pp. 407-412, doi: 10.1109/VLSID57277.2023.00086.

Manuscript in progress

1. **A. Sahni**, A. Tripathi, S. Somachi, S. Mantha, M. H. Khan, and A. Srivastava, "GoldAid: IoT-Powered Integrated Safety System with CNN for Rapid Medical

Patents

1. A. Srivastava and **A. Sahni**, "System and Method for Detecting Fall Event using Machine Learning Model in Real-time," Filed Indian Patent, Application No.: 202241066354, Nov 2022.
2. A. Srivastava, B. Ghosh, A. Sarje, **A. Sahni**, A. Tripathi, Deeksha, "A Portable System for Pneumonia Detection using Simultaneous Measurement of Vitals and Artificial Intelligence Capabilities", Filed Provisional Patent in Indian Patent Office, Application No.:202341044162, June 2023

Bibliography

- [1] Andre Bourdoux et al. “Receiver Architectures for Software-defined Radios in Mobile Terminals: the Path to Cognitive Radios”. In: *2007 IEEE Radio and Wireless Symposium*. 2007, pp. 535–538. DOI: 10.1109/RWS.2007.351886.
- [2] M. C. M. Soer et al. “A 0.2-to-2.0GHz 65nm CMOS receiver without LNA achieving > 11 dBm IIP3 and < 6.5 dB NF”. In: *2009 IEEE International Solid-State Circuits Conference - Digest of Technical Papers*. 2009, 222–223, 223a. DOI: 10.1109/ISSCC.2009.4977388.
- [3] Caroline Andrews and Alyosha C. Molnar. “Implications of Passive Mixer Transparency for Impedance Matching and Noise Figure in Passive Mixer-First Receivers”. In: *IEEE Transactions on Circuits and Systems I: Regular Papers* 57.12 (2010), pp. 3092–3103. DOI: 10.1109/TCSI.2010.2052513.
- [4] Caroline Andrews and Alyosha C. Molnar. “A Passive Mixer-First Receiver With Digitally Controlled and Widely Tunable RF Interface”. In: *IEEE Journal of Solid-State Circuits* 45.12 (2010), pp. 2696–2708. DOI: 10.1109/JSSC.2010.2077151.
- [5] Alyosha Molnar and Caroline Andrews. “Impedance, filtering and noise in n-phase passive CMOS mixers”. In: *Proceedings of the IEEE 2012 Custom Integrated Circuits Conference*. 2012, pp. 1–8. DOI: 10.1109/CICC.2012.6330616.
- [6] Dong Yang, Caroline Andrews, and Alyosha Molnar. “Optimized Design of N-Phase Passive Mixer-First Receivers in Wideband Operation”. In: *IEEE Transactions on Circuits and Systems I: Regular Papers* 62.11 (2015), pp. 2759–2770. DOI: 10.1109/TCSI.2015.2479035.
- [7] S. Hari et al. “Approaches to Nonoverlapping Clock Generation for RF to Millimeter-Wave Mixer-First Receivers”. In: *IEEE MTT-S International Microwave Conference on Hardware and Systems for 5G and Beyond (IMC-5G)*. Aug. 2019, pp. 1–3. DOI: 10.1109/IMC-5G47857.2019.9160353.

- [8] Caroline Andrews, Changhyuk Lee, and Alyosha Molnar. “Effects of LO harmonics and overlap shunting on N-phase passive mixer based receivers”. In: *2012 Proceedings of the ESSCIRC (ESSCIRC)*. 2012, pp. 117–120. DOI: 10.1109/ESSCIRC.2012.6341270.
- [9] Charley Wilson and Brian Floyd. “20–30 GHz mixer-first receiver in 45-nm SOI CMOS”. In: *2016 IEEE Radio Frequency Integrated Circuits Symposium (RFIC)*. 2016, pp. 344–347. DOI: 10.1109/RFIC.2016.7508323.
- [10] Sashank Krishnamurthy and Ali M. Niknejad. “10-35GHz Passive Mixer-First Receiver Achieving +14dBm in-band IIP3 for Digital Beam-forming Arrays”. In: *2020 IEEE Radio Frequency Integrated Circuits Symposium (RFIC)*. 2020, pp. 275–278. DOI: 10.1109/RFIC49505.2020.9218301.
- [11] Pingyue Song and Hossein Hashemi. “mm-Wave Mixer-First Receiver With Selective Passive Wideband Low-Pass Filtering”. In: *IEEE Journal of Solid-State Circuits* 56.5 (2021), pp. 1454–1463. DOI: 10.1109/JSSC.2021.3063726.
- [12] Robin Ying, Matthew Morton, and Alyosha Molnar. “A HBT-based 300 MHz-12 GHz blocker-tolerant mixer-first receiver”. In: *ESSCIRC 2017 - 43rd IEEE European Solid State Circuits Conference*. 2017, pp. 31–34. DOI: 10.1109/ESSCIRC.2017.8094518.
- [13] Jacob Dean et al. “A 4-31GHz Direct-Conversion Receiver Employing Frequency-Translated Feedback”. In: *ESSCIRC 2021 - IEEE 47th European Solid State Circuits Conference (ESSCIRC)*. 2021, pp. 187–190. DOI: 10.1109/ESSCIRC53450.2021.9567779.
- [14] Sandeep Hari et al. “Approaches to Nonoverlapping Clock Generation for RF to Millimeter-Wave Mixer-First Receivers”. In: *2019 IEEE MTT-S International Microwave Conference on Hardware and Systems for 5G and Beyond (IMC-5G)*. 2019, pp. 1–3. DOI: 10.1109/IMC-5G47857.2019.9160353.
- [15] Prateek Kumar Sharma and Nagarjuna Nallam. “Linearity and NF Tradeoff in Input-Matched N-Path Mixer-First Receivers with Shunt-Feedback TIAs”. In: *2019 IEEE International Symposium on Circuits and Systems (ISCAS)*. 2019, pp. 1–4. DOI: 10.1109/ISCAS.2019.8702176.
- [16] Susnata Mondal, Rahul Singh, and Jeyanandh Paramesh. “A reconfigurable 28/37GHz hybrid-beamforming MIMO receiver with inter-band carrier aggregation and RF-domain LMS weight

- adaptation”. In: *2018 IEEE International Solid - State Circuits Conference - (ISSCC)*. 2018, pp. 72–74. DOI: 10.1109/ISSCC.2018.8310189.
- [17] Min-Yu Huang et al. “A 24.5–43.5-GHz Ultra-Compact CMOS Receiver Front End With Calibration-Free Instantaneous Full-Band Image Rejection for Multiband 5G Massive MIMO”. In: *IEEE Journal of Solid-State Circuits* 55.5 (2020), pp. 1177–1186. DOI: 10.1109/JSSC.2019.2959495.
- [18] *BUF602 High-Speed, Closed-Loop Buffer*. Texas Instruments. May, 2008. URL: <https://www.ti.com/lit/ds/symlink/buf602.pdf>.
- [19] *NCR2-183+ 1:2 LTCC Transformer, 12000 - 18000 MHz, 50*. Mini Circuits. URL: <https://www.minicircuits.com/pdfs/NCR2-183+.pdf>.
- [20] A Soley et al. “On-line monitoring of yeast cell growth by impedance spectroscopy”. en. In: *J Biotechnol* 118.4 (Sept. 2005), pp. 398–405.
- [21] Rashi Borgohain and Sunandan Baruah. “Development and Testing of ZnO Nanorods Based Biosensor on Model Gram-Positive and Gram-Negative Bacteria”. In: *IEEE Sensors Journal* 17.9 (2017), pp. 2649–2653. DOI: 10.1109/JSEN.2017.2682920.
- [22] T. Houssin et al. “Label-free analysis of water-polluting parasite by electrochemical impedance spectroscopy”. In: *Biosensors and Bioelectronics* 25.5 (2010), pp. 1122–1129. ISSN: 0956-5663. DOI: <https://doi.org/10.1016/j.bios.2009.09.039>. URL: <https://www.sciencedirect.com/science/article/pii/S0956566309005260>.
- [23] D.K. Kamat, A.P. Chavan, and P.M. Patil. “Bio-Impedance Measurement System for Analysis of Skin Diseases”. In: *IJAIEEM* 3 (Jan. 2014), pp. 92–96.
- [24] Shruti Jha, Ritu Rani, and Sandeep Singh. “Biogenic Zinc Oxide Nanoparticles and Their Biomedical Applications: A Review”. In: *Journal of Inorganic and Organometallic Polymers and Materials* 33.6 (June 2023), pp. 1437–1452.
- [25] Sankush Krishna Maheshuni et al. “A Review on 2D-ZnO Nanostructures Based Biosensors: From Materials to Devices”. In: *Materials Advances* (Nov. 2022). DOI: 10.1039/D2MA00878E.
- [26] Ahmad Fairuzabadi Mohd Mansor and Anis Nurashikin Nordin. “Theoretical Modelling of Interdigitated Electrode Sensor for Mammalian Cell Characterization”. In: *2018 7th International*

- Conference on Computer and Communication Engineering (ICCCE)*. 2018, pp. 62–67. DOI: 10 . 1109/ICCCE.2018.8539280.
- [27] M. Ibrahim et al. “Physical and Electrical Modeling of Interdigitated Electrode Arrays for Bioimpedance Spectroscopy”. In: *New Developments and Applications in Sensing Technology*. Ed. by Subhas Chandra Mukhopadhyay, Aimé Lay-Ekuakille, and Anton Fuchs. Berlin, Heidelberg: Springer Berlin Heidelberg, 2011, pp. 169–189. ISBN: 978-3-642-17943-3. DOI: 10 . 1007 / 978 - 3 - 642-17943-3_9. URL: https://doi.org/10.1007/978-3-642-17943-3_9.
- [28] Mouhamad Ibrahim et al. “Geometric parameters optimization of planar interdigitated electrodes for bioimpedance spectroscopy”. In: *Journal of Electrical Bioimpedance* 4 (Mar. 2013), pp. 13–22. DOI: 10 . 5617 / jeb . 304.
- [29] M Paul and Sujata Sen. “The Occurrence of TDS and Conductivity of Domestic Water in Lumding Town of Nowgong District of Assam, N.E. India”. In: *Current World Environment* 7 (Dec. 2012), pp. 251–258. DOI: 10 . 12944 / CWE . 7 . 2 . 09.
- [30] “AD5933 Datasheet”. In: (). Maxim Integrated. April, 2017. URL: <https://www.analog.com/en/products/ad5933.html>.
- [31] Ummar Pasha Shaik et al. “Growth of superhydrophobic Zinc oxide nanowire thin films”. In: *Materials Letters* 75 (2012), pp. 51–53. ISSN: 0167-577X. DOI: <https://doi.org/10.1016/j.matlet.2012.01.140>. URL: <https://www.sciencedirect.com/science/article/pii/S0167577X12001826>.
- [32] Kamarul Aizat Abdul Khalid, Thye Jien Leong, and Khairudin Mohamed. “Review on Thermionic Energy Converters”. In: *IEEE Transactions on Electron Devices* 63.6 (2016), pp. 2231–2241. DOI: 10 . 1109 / TED . 2016 . 2556751.
- [33] Ravikumar Sanapala et al. “Effect of Lead-Free Soldering on Key Material Properties of FR-4 Printed Circuit Board Laminates”. In: *IEEE Transactions on Electronics Packaging Manufacturing* 32.4 (2009), pp. 272–280. DOI: 10 . 1109 / TEPM . 2009 . 2029566.
- [34] Gabriel N. Meloni. “Building a Microcontroller Based Potentiostat: A Inexpensive and Versatile Platform for Teaching Electrochemistry and Instrumentation”. In: *Journal of Chemical Education* 93.7 (2016), pp. 1320–1322. DOI: 10 . 1021 / acs . jchemed . 5b00961.

- [35] Younas Iqbal et al. "Orientation and actual growth mechanism of ZnO nanorods through hydrothermal method on gold seed layer". In: *AIP Advances* 11.12 (Dec. 2021), p. 125006. ISSN: 2158-3226. DOI: 10.1063/5.0067231. eprint: https://pubs.aip.org/aip/adv/article-pdf/doi/10.1063/5.0067231/12930537/125006_1_online.pdf. URL: <https://doi.org/10.1063/5.0067231>.
- [36] *Permissible levels of certain chemical substances in work environment*. URL: <https://dgfasli.gov.in/en/book-page/permissible-levels-certain-chemical-substances-in-work-environment>.
- [37] "Mine Safety and Health Administration (MSHA). Heat Stress in Mining." In: (). URL: <https://www.msha.gov/heat-stress>.
- [38] "World Statistic by ILO." In: (). URL: https://www.ilo.org/moscow/areas-of-work/occupational-safety-and-health/WCMS_249278/lang--en/index.htm.
- [39] Evan A Nadhim et al. "Falls from Height in the Construction Industry: A Critical Review of the Scientific Literature". en. In: *Int J Environ Res Public Health* 13.7 (June 2016).
- [40] "TCS IoT Safety Watch". In: (). URL: <https://iot.tatacommunications.com/product/safety-watch>.
- [41] "Spot-r." In: (). URL: <https://www.triaxtec.com/resource/fact-sheet/spot-r-mesh/>.
- [42] "Tended Wearable". In: (). URL: <https://tended.co.uk/>.
- [43] "BlackLine G7 Lone Worker Monitor". In: (). URL: <https://www.blacklinesafety.com/solutions/lone-worker/g7-lone-worker>.
- [44] "Reactec RASOR." In: (). URL: <https://www.reactec.com/workplace-risk-prevention/lone-workers/>.
- [45] "Lifecall Advanced Mobile." In: (). URL: <https://www.lifecall.com/products/AdvancedMobile>.
- [46] Denisse Castaneda et al. "A review on wearable photoplethysmography sensors and their potential future applications in health care". In: *International journal of biosensors & bioelectronics* (2018), pp. 195–202. ISSN: 2573-2838. DOI: 10.15406/ijbsbe.2018.04.00125.

- [47] Saquib et al. “Measurement of heart rate using photoplethysmography”. In: *2015 International Conference on Networking Systems and Security (NSysS)*. 2015, pp. 1–6. DOI: 10.1109/NSysS.2015.7043525.
- [48] Devarshi Mrinal Das et al. “A pulse oximeter system, OxiSense, with embedded signal processing using an ultra-low power ASIC designed for testability”. In: *Microelectronics Journal* 72 (2018), pp. 1–10.
- [49] Bard et al. “Cuff-Less Methods for Blood Pressure Telemonitoring”. In: *Frontiers in Cardiovascular Medicine* 6 (2019), p. 40. ISSN: 2297-055X. DOI: 10.3389/fcvm.2019.00040.
- [50] Dave Knight. “Lithium Ion Cell Protection”. In: (). URL: <https://www.digikey.in/en/maker/blogs/lithium-ion-cell-protection>.
- [51] LoRaWAN. <https://www.thethingsnetwork.org/docs/lorawan/>.
- [52] Lim et al. “Fall-Detection Algorithm Using 3-Axis Acceleration: Combination with Simple Threshold and Hidden Markov Model”. In: *Journal of Applied Mathematics* 2014 (Sept. 2014), p. 896030. ISSN: 1110-757X.
- [53] Bouten et al. “A triaxial accelerometer and portable data processing unit for the assessment of daily physical activity”. en. In: *IEEE Trans Biomed Eng* 44.3 (Mar. 1997), pp. 136–147.
- [54] Sucerquia et al. “SisFall: A Fall and Movement Dataset”. en. In: *Sensors (Basel)* 17.1 (Jan. 2017).
- [55] Miller et al. “An envelope of linear and rotational head motion during everyday activities”. In: *Biomechanics and Modeling in Mechanobiology* 19.3 (June 2020), pp. 1003–1014. DOI: 10.1007/s10237-019-01267-6. eprint: 1911.12604. URL: <https://doi.org/10.1007/s10237-019-01267-6>.
- [56] Palmerini et al. “Accelerometer-Based Fall Detection Using Machine Learning: Training and Testing on Real-World Falls”. In: *Sensors* 20.22 (2020). ISSN: 1424-8220. DOI: 10.3390/s20226479.
- [57] Kanghyeok Yang et al. “Semi-supervised near-miss fall detection for ironworkers with a wearable inertial measurement unit”. In: *Automation in Construction* 68 (2016), pp. 194–202. ISSN: 0926-5805. DOI: <https://doi.org/10.1016/j.autcon.2016.04.007>.
- [58] Santos et al. “Accelerometer-Based Human Fall Detection Using Convolutional Neural Networks”. In: *Sensors* 19.7 (2019). ISSN: 1424-8220.

- [59] Cruciani et al. “Comparing CNN and Human Crafted Features for Human Activity Recognition”. In: *2019 IEEE SmartWorld, (SmartWorld/SCALCOM/UIC/ATC/CBDCOM/IOP/SCI)*. 2019, pp. 960–967. DOI: 10.1109/SmartWorld-UIC-ATC-SCALCOM-IOP-SCI.2019.00190.
- [60] Youssef Abadade et al. “A Comprehensive Survey on TinyML”. In: *IEEE Access* 11 (2023), pp. 96892–96922. DOI: 10.1109/ACCESS.2023.3294111.
- [61] Abien Fred Agarap. *Deep Learning using Rectified Linear Units (ReLU)*. 2019. arXiv: 1803.08375 [cs.NE].
- [62] Rok Blagus and Lara Lusa. “SMOTE for high-dimensional class-imbalanced data”. In: *BMC Bioinformatics* 14.1 (Mar. 2013), p. 106. ISSN: 1471-2105.
- [63] Ning Jia. “Detecting Human Falls with a 3-Axis Digital Accelerometer”. In: (). URL: <https://www.analog.com/en/analog-dialogue/articles/detecting-falls-3-axis-digital-accelerometer.html>.
- [64] *MPU6050 MotionTracking Device*. Invensense. Rev. 3.4, Aug, 2013.
- [65] Hascoet et al. “Layer-Wise Invertibility for Extreme Memory Cost Reduction of CNN Training”. In: *2019 IEEE/CVF International Conference on Computer Vision Workshop (ICCVW)*. 2019, pp. 2049–2052. DOI: 10.1109/ICCVW.2019.00258.
- [66] eloquentarduino. *tinymlgen*. <https://github.com/eloquentarduino>.
- [67] “Occupational Safety and Health Administration (OSHA), Carbon Monoxide Poisoning - Quick Facts”. In: (). URL: <https://www.osha.gov/sites/default/files/publications/carbonmonoxide-factsheet.pdf>.
- [68] Protocentral. *Pulse Express Pulse-Ox Heart Rate Sensor with MAX32664*. URL: <https://protocentral.com/product/pulse-express-pulse-ox-heart-rate-sensor-with-max32664/>.
- [69] Pelaez et al. “LED power reduction trade-offs for ambulatory pulse oximetry”. In: *2007 29th Annual International Conference of the IEEE Engineering in Medicine and Biology Society*. 2007, pp. 2296–2299. DOI: 10.1109/IEMBS.2007.4352784.
- [70] *MAX30102 High-Sensitivity Pulse Oximeter and Heart-Rate Sensor for Wearable Health*. Maxim Integrated. Oct, 2018.

- [71] *MAX32664 Ultra-Low Power Biometric Sensor Hub*. Maxim Integrated. Rev. 3, Oct, 2018.
- [72] *High-Accuracy, Low-Power, Digital Temperature Sensor*. Texas Instruments. Rev. D, September, 2022.
- [73] Ebrahimi et al. “Ultralow-Power Photoplethysmography Sensors: A Methodological Review”. In: *IEEE Sensors Journal* 23.15 (2023). DOI: 10.1109/JSEN.2023.3284818.
- [74] *ESP32-WROOM-32*. Espressif Systems. Rev. 2.3.
- [75] *LoRa Module*. Ai-Thinker. Rev. 1.1, Aug, 2013.
- [76] Aziz et al. “A comparison of accuracy of fall detection algorithms (threshold-based vs. machine learning) using waist-mounted tri-axial accelerometer signals from a comprehensive set of falls and non-fall trials”. en. In: *Med Biol Eng Comput* 55.1 (Apr. 2016), pp. 45–55.